

**INVESTIGATING MULTI-DECadal ATMOSPHERE & OCEAN
VARIABILITY**

by

Jordan L. Thomas

A dissertation submitted to Johns Hopkins University in conformity
with the requirements for the degree of Doctor of Philosophy

Baltimore, MD
February 2018

©2018 Jordan L. Thomas
All rights reserved

Abstract

Lorem ipsum dolor sit amet, consectetur adipiscing elit. Donec malesuada turpis lorem, a malesuada nulla mollis non. Cras et enim id dui viverra pharetra nec a orci. Aenean malesuada mi arcu, vel mollis diam bibendum ac. Duis lorem quam, euismod id tellus ac, consequat tempor eros. Morbi tempor eu lacus non feugiat. In vel feugiat urna. Curabitur faucibus metus ac fringilla convallis. Aliquam non aliquet dui. Morbi sed nunc ut sem egestas malesuada.

Nulla condimentum dictum nisl sed sollicitudin. Morbi fermentum lobortis congue. Suspendisse lobortis dui eget nunc dictum maximus. Vestibulum ullamcorper leo nec sagittis iaculis. Duis diam dolor, facilisis sit amet vulputate pellentesque, tempus et sem. Pellentesque in ipsum ut metus ullamcorper hendrerit. Phasellus quam turpis, tristique in dictum a, cursus vitae justo. Duis feugiat tincidunt justo, volutpat convallis ligula tristique id. Pellentesque quis nibh commodo, semper quam vel, ultrices neque. Nam auctor commodo ipsum dapibus scelerisque. Duis rhoncus eros at pretium convallis.

Morbi placerat fermentum ex a porttitor. Vivamus rhoncus massa vel ex laoreet tincidunt. Etiam sit amet leo iaculis, posuere lacus ac, pretium felis. Aenean nisl leo, condimentum eu placerat ullamcorper, mollis quis neque. In ut porttitor quam. Pellentesque ac sapien in lorem posuere convallis. Suspendisse efficitur massa ac mollis luctus. Aliquam a pharetra purus. Mauris quam sem, scelerisque maximus urna non, imperdiet dictum enim. Vestibulum quis fringilla metus.

Etiam tempus odio in magna placerat maximus. Pellentesque efficitur, orci eu vulputate auctor, neque metus suscipit libero, id consequat ante ante sit amet

diam. Donec ut posuere elit, nec feugiat orci. Mauris at ipsum et quam finibus dictum vel et lorem. Aliquam et nulla dignissim, egestas orci vel, pellentesque purus. Suspendisse a libero vitae libero accumsan viverra vulputate nec nunc. Proin ultrices nulla eget accumsan efficitur. Duis vel sem luctus, vulputate risus sit amet, pretium tortor. Etiam eleifend.

Faculty Advisor and First Reader: Professor Darryn Waugh
Earth and Planetary Science Department, Johns Hopkins University

Second Reader: Professor Anand Gnanadesikan
Earth and Planetary Science Department, Johns Hopkins University

Acknowledgements

Lorem ipsum dolor sit amet, consectetur adipiscing elit. Ut posuere vehicula ligula a aliquet. Fusce imperdiet augue sapien. Suspendisse consequat ipsum a pulvinar bibendum. Morbi tincidunt non lorem mollis euismod. Nulla sit amet leo elementum, venenatis mi vel, finibus turpis. Curabitur fermentum tellus porta orci commodo, id cursus elit bibendum. Sed venenatis lacus nec malesuada posuere. Fusce at libero quis orci faucibus malesuada vitae quis nibh. Nunc sem odio, faucibus vel mauris id, ultricies luctus augue. Sed venenatis arcu eu augue luctus fringilla. Curabitur tincidunt metus et tellus eleifend, et consequat massa accumsan. Integer rutrum ullamcorper dignissim. Aenean cursus consectetur bibendum. Nulla et eros eu sapien tincidunt dapibus non vel tortor.

Curabitur tincidunt risus ut nibh sollicitudin, id luctus nunc imperdiet. Morbi ultrices viverra ex non facilisis. Integer ac auctor neque. Proin nisl leo, aliquet sed augue a, sollicitudin placerat dolor. Fusce ac auctor sapien, id pellentesque justo. Vestibulum faucibus.

Contents

1	Introduction	1
1.1	Natural Variability	1
1.1.1	What is Natural Variability?	1
1.1.2	Why is natural variability important?	2
1.1.3	Challenges quantifying natural variability?	3
1.2	Background	3
1.2.1	Surface Mixed Layer	3
1.2.2	Ocean Circulation	4
1.2.3	High latitude atmospheric circulation and the impact on the ocean.	5
1.2.4	Ocean Biogeochemistry	5
1.3	Overview and Aims	5
2	Recent trends and natural variability	7
2.1	Overview and aims	7
2.2	Methods	8
2.3	Results & Discussion	12
2.3.1	Natural Variability	12
2.3.2	Observed trends	13
2.3.3	Model historical trends	16
2.4	Conclusions	17
3	Ocean heat and carbon variability	20
3.1	Introduction	20
3.2	Methods	22
3.2.1	Model and Simulation Descriptions	22
3.2.2	Heat and Carbon Content	26
3.2.3	Surface Heat Flux	26
3.2.4	Southern Ocean	28
3.3	Temporal and Spatial Variations in Heat and Carbon Content	28
3.3.1	Weddell Sea Convection	28

3.3.2 Global Heat and Carbon Variability	31
3.3.3 Regional Heat and Carbon Variability	36
3.4 Mechanisms Driving Variability	39
3.4.1 Heat Content Variability	39
3.4.2 Carbon Content Variability	40
3.5 Conclusions	45
4 Relationship between age and oxygen	50
4.1 Abstract	50
4.2 Introduction	51
4.3 Methods	53
4.3.1 Line W Observational Data	53
4.3.1.1 Data Collection	53
4.3.1.2 Data Processing	54
4.3.1.3 Mean Age Calculation	55
4.3.2 Model Data	57
4.4 Results	58
4.4.1 Age and Oxygen Relationship	58
4.4.2 Age and Oxygen/AOU Scatterplots	64
4.4.3 Mechanisms Driving Age and Oxygen Variability	67
4.4.3.1 Horizontal Extent of Anomalous Correlation	67
4.4.3.2 Line W versus Line 40N	69
4.5 Conclusions	73
Bibliography	76

List of Tables

2.1	CMIP 5 models used in this study.	9
2.2	Probability of obtaining averaged reanalysis trend by only natural variability (first three columns) and natural variability + historical multi-model ensemble trend (second three columns).	13
3.1	Relationship between Weddell Sea subsurface temperature and global carbon and heat content anomalies. All correlations are statistically significant from 0 ($p = 0.005$).	34

List of Figures

2.1	SAM time-series for (a) MPI ESM MR and (c) MIROC5 piControl runs over the first 100 years. The red lines indicate periods where the trend is greater than the average reanalysis trend between 1980-2004. Figures b and d show the probability density functions for the 25-year linear SAM trends in MPI ESM MR and MIROC5 respectively. The blue dot represents the mean of the 25-year trends while the whiskers extend 2 standard deviations. The vertical lines represent the observed trends: NCEP R1 (green), NCEP R2, ERA-Int, and JRA-55 (black), and the red asterisk shows the magnitude of the historical model run trend (first ensemble member).	10
2.2	Natural variability, historical trends and observations for (a) SAM, (b) 850mb jet latitude, (c) wind-stress jet latitude, (d) 850mb jet magnitude, and (e) wind-stress jet magnitude. Blue circles show the mean of the pi-Control 25-year linear trends indicating model drift. Whisker length is 2 standard deviations. Red points show the historical run trends for each ensemble member. Horizontal dashed lines indicate the absolute value of the observed trends: NCEP R1 (green), NCEP R2 (orange), ERA-Int (purple), and JRA-55 (black).	14
2.3	Correlation coefficient squared for correlation of the the 25-year linear trends in wind-stress jet location, wind-stress jet magnitude, 850mb jet location, and 850mb jet magnitude with the 25-year trends in SAM for each model.	18

3.1	Comparison of control (blue), low eddy diffusion (purple), high eddy diffusion (red), and high eddy advection (green) simulations. JJA Southern Ocean (60–90°S) (a) temperature (b) salinity and (c) density stratification ($\sigma_0 - \sigma_0^{1500m}$). (d) JJA zonal surface wind stress and (e) Antarctic sea ice extent. Observational data for each metric is shown in black. Temperature, salinity, density stratification are estimates from the 2001 World Ocean Atlas 2001 dataset [Boyer <i>et al.</i> , 2002]. Surface wind stress are from ERA-Interim and averaged between 1979–2015. Sea extent is calculated using the National Snow and Ice Data Center Sea Ice Index [Fetterer <i>et al.</i> , 2016] .	25
3.2	Correlation between (a) vertically integrated carbon content at each location and global carbon content and (b) vertically integrated heat content at each location and global heat content for the control simulation ($A_{\text{redi}} = 800 \text{ m s}^{-2}$)	27
3.3	Annually averaged subsurface temperature (color contours) and mixed layer depth (solid black line) averaged over Weddell Sea for (a) Control simulation ($A_{\text{redi}} = 800 \text{ m s}^{-2}$), (b) Low Eddy Diffusion simulation ($A_{\text{redi}} = 400 \text{ m s}^{-2}$), (c) High Eddy Diffusion simulation ($A_{\text{redi}} = 2400 \text{ m s}^{-2}$), and (d) High Eddy Advection simulation ($GM_{\min} = 600 \text{ m s}^{-2}$)	30
3.4	Carbon content anomaly, heat content anomaly and Weddell Sea subsurface temperature (averaged between 1500–2000 m, 0°–60°W, 60°–80°S) for control simulation. Blue circles indicate beginning of convection and red circles indicate end of convection defined using four strongest local maxima and minima in Weddell Sea Subsurface Temperature.	32
3.5	Globally integrated carbon content anomaly (black) and heat content anomaly (red) for (a) Control simulation ($A_{\text{redi}} = 800 \text{ m s}^{-2}$), (b) Low Eddy Diffusion simulation ($A_{\text{redi}} = 400 \text{ m s}^{-2}$), (c) High Eddy Diffusion simulation ($A_{\text{redi}} = 2400 \text{ m s}^{-2}$), and (d) High Eddy Advection simulation ($GM_{\min} = 600 \text{ m s}^{-2}$)	33
3.6	Pearson correlation coefficients for integrated carbon content anomaly versus integrated heat content anomaly for each region.	35
3.7	Linear regression of each region's carbon content against global carbon content (blue) and each regions heat content against global heat content (red). Linear regression 95% confidence interval is shown, but too small to be discerned.	37
3.8	Subsurface (a) potential temperature, (b) DIC, (c) remineralized DIC, and (d) preformed DIC for convective year composite from control simulation. Only the surface ocean is shown to highlight the strongest-magnitude features.	38
3.9	Top: Weddell Sea subsurface temperature as in Figure 3.4 (green) and Weddell Sea mixed layer depth (black). Bottom: Southern Ocean surface heat flux where positive indicates into the ocean (red), Southern Hemisphere SST averaged between 0°–55°S (blue) for the control simulation.	40

3.10 Scatter of heat content anomaly vs preformed DIC integrated over the tropical region for each simulation. Dashed grey linear line represents the linear fit of the carbon vs heat data with slope, m , and pearson correlation coefficient r . Solid black linear line represents the projected change in carbon content given a change in heat content with constant alkalinity and $p\text{CO}_2$ in equilibrium with the preindustrial atmosphere (scaled from <i>Gruber et al.</i> [1996]).	42
3.11 Ideal age versus remineralized DIC for all simulations. Quantities are averaged over latitudes 40° – 50°S and 200–1000 m. Linear regression coefficients, m , and pearson correlation coefficients, r , are included for reference.	44
3.12 Covariance between globally integrated DIC content and DIC (black), preformed DIC (blue) and remineralized DIC (red) for each simulation as a function of latitude. Note different y-axis scales.	45
3.13 Schematic summarizing regional variability in oceanic heat and carbon during a convective year. Arrows designate the sense of global and regional inventory change during a convective year, positive indicating an increase in oceanic content.	47
4.1 Observational Line W and model interpolation. (a) and (b) climatologies of observational temperature and salinity. (c) and (d) Line W interpolated model temperature and salinity.	54
4.2 Observational age and oxygen for two years.	56
4.3 (a) Oxygen climatology and (b) age climatology from observations along Line W. Contour lines show average neutral density.	59
4.4 Pearson correlation coefficients for age versus (left) oxygen and (right) AOU for Line W observations. Contour lines indicate average neutral density climatology.	63
4.5 Correlation between age and AOU on various isopycnal surfaces. Left column indicate correlation calculated on average depth of the isopycnal surface, and therefore including contributions from isopycnal heave. Right column shows correlation calculated on the isopycnal surface and does not include contributions from heave.	68
4.6 Climatologies of (a) age and (b) AOU interpolated on neutral density surface 27.0. Bottom: Standard deviation of (c) age tendency and (d) AOU tendency interpolated on neutral density surface 27.0. Bottom plots are calculated as the standard deviation of the first term on right-hand side of equation (4).	70
4.7 Age-AOU correlation and vertical profiles for (top) Line W and (bottom) Line 40N.	72
4.8 Circulation on neutral density surface 27.0	74

CHAPTER 1

Introduction

1.1 Natural Variability

1.1.1 *What is Natural Variability?*

One of the primary challenges of assessing the impact of anthropogenic influence on Earth's climate is a lack of understanding of the natural fluctuations of the climate system. Internal climate variability is simply how Earth's climate varies in time without any external forcing. External forcing can be natural in source, including volcanic eruptions, and solar forcing, or anthropogenic, including human emissions of greenhouse gases and human caused land use changes. The term natural variability on the other hand is typically used to refer to fluctuations in Earth's climate caused solely by natural forcing (internal or external), and not including anthropogenic influence.

Natural variations in the climate system, also referred to as 'climatic noise', (Madden 1976; Schneider and Kinter 1994; Wunsch 1999; Feldstein 2000) are a result of non-linear dynamical and biological processes in the atmosphere and ocean operating on a variety of spatial and temporal scales. The most common example of natural variability is the

1.1. NATURAL VARIABILITY

El Niño-Southern Oscillation (ENSO), which is a result from the non-linear interactions between the atmosphere and ocean in the Equatorial Pacific. ENSO in turn impacts temperatures across much of the Northern Hemisphere, further interacting with other modes of variability.

A further complicating matter is that climate variations happen on all timescales: paleoclimatic, centennial, multi-decadal, decadal, interannual, seasonal, and on all spatial scales from regional to global.

1.1.2 *Why is natural variability important?*

Quantification of natural variability is important to climate science for many reasons. First, natural variability is key to determine climate predictability. Climate predictability was first defined in 1975 (Academy of sciences publication) as a measure of signal-to-noise, where the signal is any potentially predictable long-term (> 1 year) climate feature, and the noise is natural variability. (Answering the question - how large does a trend need to be in order to detect it?) Projection uncertainty.

Another example of where understanding natural variability is important is in the evaluation of global climate models. Because of observational limitations and the inability to experiment on the entire earth system, climate models are developed and used to further our knowledge of the planet and climate system. Climate models are typically validated against the mean state of a given climate feature. For example, to assess the accuracy of the ocean module in a climate model, one might compare the average sea surface temperature (SST) in a pre-industrial control model run to the average of many years of SST observations from similar period (via proxy records). While this method is useful for assessing the mean state of the climate model, it does not give any information about the variability of the model. The model could have vastly larger variance than the observations, which would not be captured in comparing the means.

1.1.3 *Challenges quantifying natural variability?*

1.2 Background

As the largest reservoir for carbon and heat in the Earth system on decadal-to-centennial timescales (Figure 1.1), the ocean has a great amount of influence on global climate variability (referencesâ€).

1.2.1 *Surface Mixed Layer*

The atmosphere and ocean primarily interact through gas exchange in the surface mixed layer of the ocean. This top layer of the ocean is mixed and stirred by the overlying atmospheric winds. This mechanical forcing acts to create a layer that is nearly uniform with respect to the vertical tracer gradient. Gas exchange between the atmosphere and ocean is determined by atmosphere-ocean disequilibrium. For oceanic heat content, it is the disequilibrium between the atmosphere temperature and mixed layer ocean temperature that determines if heat is transfer between the two mediums. For carbon dioxide, it is the partial pressure of CO₂, pCO₂, that drives the gas exchange between the atmosphere and ocean.

Tracer concentrations in the surfaced mixed layer are balanced by this atmosphere-ocean gas exchange at the surface, lateral and vertical advection of the tracers, and tracer diffusion (ref). Lateral advection is primarily driven by the winds at the surface whereas vertical advection typically acts through entrainment at the base of the mixed-layer. Entrainment occurs when the depth of the mixed layer varies with time (typically the seasonal cycle). While diffusive fluxes in the surface mixed layer are usually much smaller compared to the other terms (Levy et al., 2013).

1.2.2 *Ocean Circulation*

The circulation of the surface ocean is primarily driven by the meridional gradient in the zonal surface winds. Because the zonal winds vary with latitude, the winds impart local vorticity (i.e. spin) into the ocean. This momentum, combined with the Earth's rotation (planetary vorticity, i.e. Coriolis force), sets up circular flow pattern in the ocean basins with anti-cyclonic flow in the subtropical-gyres (counter-clockwise in the NH) and cyclonic flow in the tropical and polar gyres (clockwise in the NH) with intensification on the westward side of the ocean basin. This balance between the vorticity imparted by the wind-stress and the planetary vorticity is referred to as Sverdrup's balance (Sverdrup 1947). Ekman transport (Ekman 1905) results in net transport at a right angle to the surface current (in Northern Hemisphere) resulting in water converging at the center of the sub-tropical basin gyres.

Southern Ocean is unique because it is the only area in the global Oceans where the ocean extends around the entire globe. Additionally, this ocean is aligned with the overlying sub-tropical westerly jet. The result is a surface current which wraps around the entire globe, the Antarctic Circumpolar Current, with an average strength of 130 Sv.

Via Ekman pumping, the westerly winds over the Southern Ocean transport water northwards that forces water from depth up to the surface, causing shoaling of isopycnals (density surfaces). Due to the northward volume transport of water, the Southern Ocean forms a key area in the large-scale overturning circulation in the ocean.

While it's the interaction of the oceanic surface waters and the atmosphere that drive the air-ocean exchange of tracers, it's the transport of these tracers into the deep ocean that allows the ocean to function as such a substantial sink for atmospheric quantities (most notably carbon and heat). This exchange of surface water into the deeper ocean, requires a substantial change in density (densification), while the exchange of deep water to the surface typically requires strong mechanical forcing (i.e. wind forcing).

Because of these requirements, this surface-deep water exchange localized to only a few places in the global ocean - usually in the high latitudes.

Southern Ocean Circulation

1.2.3 *High latitude atmospheric circulation and the impact on the ocean.*

1.2.4 *Ocean Biogeochemistry*

This chapter gives an idea of how complex and interrelated the atmosphere and ocean climate system is, and why understanding natural climate oscillations is so important. In the next section, the detailed aims of this thesis are discussed, and the structure is outlined.

1.3 Overview and Aims

This thesis takes an investigative look at the multi-decadal natural variability of three important components of the climate system: the SH westerly jet, oceanic carbon and heat content, and North Atlantic oxygen and age. These three components of the atmosphere and ocean variability were selected because of the important role they have in the response of the global climate system.

In Chapter 2, multiple state-of-the-art global climate models are examined in order to quantify the natural variability of the SH westerly jet. This natural variability is then compared with recent observational trends that have been attributed to anthropogenic activities. This analysis provides insight into the climatic predictability of the SH westerly jet.

Another incredibly important feature of climate variability is the variability of oceanic carbon and heat content. In Chapter 3, a single Earth System Model is deployed to investigate the variability of both oceanic carbon and heat content and the relationship between

1.3. OVERVIEW AND AIMS

the two quantities.

In Chapter 4,

Finally, conclusions in Chapter 5.

CHAPTER 2

Recent trends and natural variability

The work contained in this chapter is based upon *Thomas et al.* [2015], published in *Geophysical Research Letters*.

2.1 Overview and aims

The Southern Ocean plays a critical role in the ocean overturning circulation and moderating global climate through carbon and heat uptake [??], with approximately 40% of anthropogenic carbon and 75% of heat entering the ocean south of 30°S [*Frölicher et al.*, 2014a; *Sabine et al.*, 2004]. The leading mode of Southern Hemisphere (SH) extratropical variability, the Southern Annular Mode (SAM), has been shown to directly affect this overturning circulation and the distribution of anthropogenic carbon uptake by altering the magnitude and location of the westerly jet [???]. It is therefore important to understand the variability in the SH extratropical circulation.

Observations and reanalyses have shown a positive trend in SAM and jet magnitude over the last couple decades along with a poleward shift in the jet location [??] in addition to trends in subtropical sea surface temperature, Antarctic sea ice extent, ocean ventila-

2.2. METHODS

tion and gyre circulation [??*Waugh et al.*, 2013; ?]. Additionally, studies have detected anthropogenic influences in surface pressure and the westerly jet [??]. These trends in the SAM and consequently the jet have been largely attributed to ozone depletion in the SH stratosphere during austral summer [???]. However, there is also evidence that this positive phase trend in the SAM is due in part to greenhouse gas warming [???].

While there is evidence of anthropogenic forcing, understanding the forcing in the context of natural variability is difficult given the lack of in-situ observations and satellite information prior to 1979. Previous studies have tried to quantify the natural variability in the SH using proxy records [??] and climate models [*Latif et al.*, 2013]. Understanding the relative contribution of natural variability and anthropogenic forcing to recent trends is critical to understanding how global climate will be influenced in the future.

In this study, we aim to further estimate the natural variability of the SH extratropical circulation by using the Coupled Model Intercomparison Project Phase 5 (CMIP5) pre-industrial control model runs. We examine five metrics of the SH extratropical circulation: the SAM, the jet location defined using the 850mb winds (U_{lat}) and the surface wind-stress (τ_{lat}), the jet magnitude defined by the 850mb winds (U_{max}) and the surface wind-stress (τ_{max}). We turn to CMIP5 pre-industrial model runs to quantify the natural variability of these five metrics to address the following questions: Can recently observed trends in SH circulation occur in CMIP5 piControl model runs due to natural variability alone, do the CMIP5 models historical (1980-2004) runs show significant trends in the circulation metrics, and do these simulated historical trends capture the characteristics of the observed trends?

2.2 Methods

In order to examine the natural multi-decadal-scale variability in the SH circulation we use a combination of pre-industrial control (“piControl”) and historical (1980 to 2004)

2.2. METHODS

TABLE 2.1: CMIP 5 models used in this study.

Model	piControl (years)	model	run length	Historical runs	model	ensemble
CanESM2	996			1		
CNRM CM5	850			10		
GFDL ESM2M	500			1		
IPSL CM5a LR	1000			6		
IPSL CM5a MR	300			3		
IPSL CM5b LR	300			1		
MIROC ESM	531			3		
MIROC ESM CHEM	255			1		
MIROC5	200			5		
MPI ESM LR	1000			3		
MPI ESM MR	1000			3		
MRI CGCM3	500			3		
NOR ESM1m M	501			1		
NOR ESM1m ME	252			1		

runs from models. Table 1 lists the models used in this study, the length of their piControl run and the number of historical runs. The models were chosen based on the availability of monthly-mean fields of sea level pressure, 850mb zonal winds and zonal wind-stress for both piControl and historical runs. We focused on the austral summer (averaged over December, January and February) because this is the season where the largest trends are observed [??].

From the monthly sea-level pressure, we calculated the SAM as the zonal sea level pressure difference between 65° and 40° degrees South. For the sake of comparisons across different models, we chose to leave the SAM as a surface pressure difference as opposed to normalizing by the standard deviation as done in ? to avoid normalizing by different standard deviations across models. Additionally, we examine the SH westerly jet magnitude and location calculated using both zonal surface wind-stress (τ_{max} and τ_{lat}) and 850mb zonal winds (U_{max} and U_{lat}). To find the jet maximum and location, the maximum zonal-mean wind-stress/850mb winds and the surrounding 4 grid-points were isolated and interpolated to a 0.1-degree meridional grid. A quadratic polynomial was then fit to the interpolated data and the maximum magnitude and location was found.

2.2. METHODS

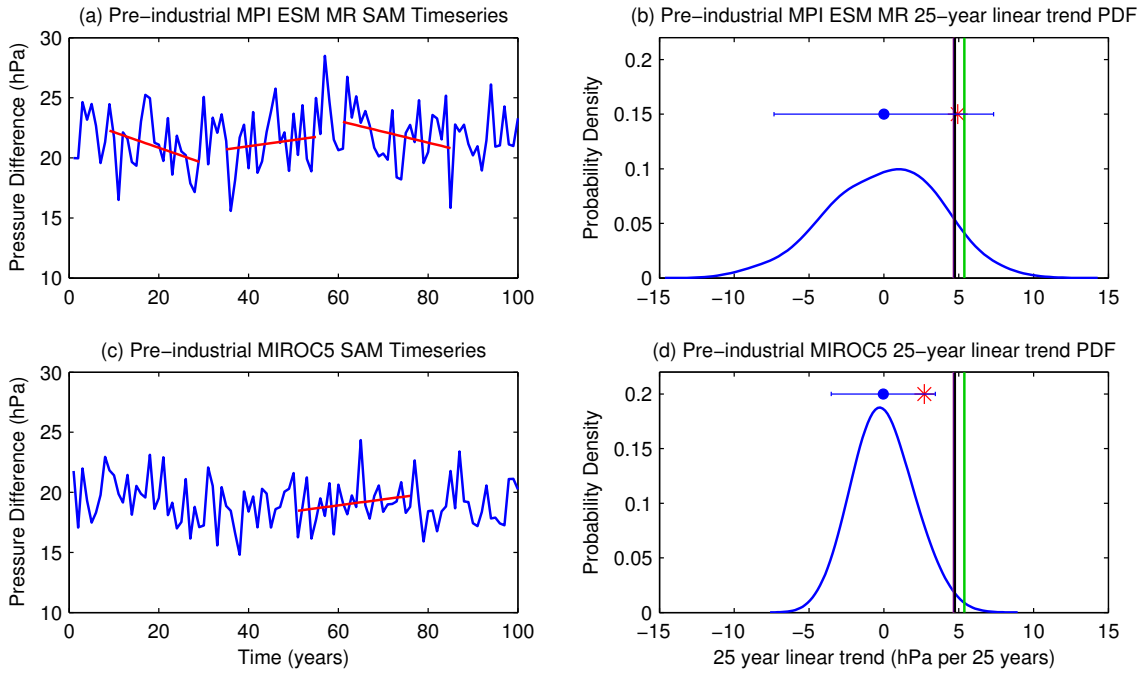


FIGURE 2.1: SAM time-series for (a) MPI ESM MR and (c) MIROC5 piControl runs over the first 100 years. The red lines indicate periods where the trend is greater than the average reanalysis trend between 1980-2004. Figures b and d show the probability density functions for the 25-year linear SAM trends in MPI ESM MR and MIROC5 respectively. The blue dot represents the mean of the 25-year trends while the whiskers extend 2 standard deviations. The vertical lines represent the observed trends: NCEP R1 (green), NCEP R2, ERA-Int, and JRA-55 (black), and the red asterisk shows the magnitude of the historical model run trend (first ensemble member).

While there are no trends (i.e., drift) in these metrics over the length of the piControl time-series (order 250-1000 years), strong multi-decadal trends are found. Time-series in SAM from a high-varying model (MPI ESM MR) and a low-varying model (MIROC5) are shown in Figure 2.1a and c respectively. As highlighted in red, there are multiple 25-year periods that have strong trends even though there is no trend over the entire time-series. In order to quantify the variability of these multi-decadal-scale trends, we calculate the linear trend of each metric (SAM, τ_{max} , τ_{lat} , U_{max} , and U_{lat}) for consecutive and overlapping 25-yr trends for each model's piControl run (? performed a similar analysis for sea ice extent in piControl runs).

We focus on the period 1980-2004 because reanalyses are unreliable before the implementation of satellites in 1979 (? Figure 1). Our analysis goes up until 2004 in order to

2.2. METHODS

compare with the CMIP5 historical model runs, which are typically run until year 2005. To verify that period length does not influence our results, the same analysis with CMIP5 piControl model runs and observations for the 34-year period between 1980-2014 was conducted (not shown). The results are essentially identical to those reported below as the observed changes over this period are either the same size or smaller than over the 1980-2005 period and the modeled trends are only slightly smaller.

The distribution of these 25-yr trends for the model piControl run is a measure of the natural multi-decadal variability in each model (in other words, the model internal variability with no anthropogenic influences). As an example, the probability density function (PDF) of these 25-year linear trends for the MPI ESM MR and MIROC5 models are shown in Figure 1b and d. The blue curve shows the probability density of the 25-year linear trends for the SAM, and the whisker plot shows the mean (blue circle) and 2 standard deviations (whisker extent) of the 25-year trends. The means of the 25-year trends (blue dot) are near zero, consistent with there being no drift in the piControl runs, but the trend for any individual 25-year period varies from -10 to +10 hPa per 25 yrs (with standard deviation of around 4 hPa per 25 yrs). Throughout the rest of the paper we shall use the whiskers to represent the distribution of 25-year trends from the model piControl runs. Each CMIP5 model has a different piControl run length, which could potentially impact our model-model comparisons. However, subsampling the output from 1000 year piControl runs shows limited sensitivity of the standard deviation of 25-yr trends for run lengths between 250 and 1000 yrs.

To compare the observations with the modeled natural variability, we used four reanalysis products: NCEP Reanalysis 1 (NCEP-1) [?], NCEP Reanalysis 2 (NCEP-2) [?], ERA-Interim [?], and JRA-55 [?] during the period 1980-2004. We also calculated the linear trend between the years 1980-2004 from the model historical runs, and compared both with the observed trends and model natural decadal variability. The vertical lines in Figure 1b and d represent the 1980-2004 reanalysis trends and the red asterisk shows

2.3. RESULTS & DISCUSSION

historical simulation trend.

2.3 Results & Discussion

2.3.1 Natural Variability

We first examine the distribution of 25-year linear trends from CMIP5 piControl runs. Figure 2 shows, as whisker plots, the distributions of 25-year linear trends of (a) SAM, (b) U_{lat} , (c) τ_{lat} , (d) U_{max} , and (e) τ_{max} , for each model. For all five metrics, the mean 25-year linear trend (blue circles) is around zero for all the models, as expected for unforced model runs with no drift. The width of the whiskers is, however, variable across the different models, indicating differences in the multi-decadal variability among the models. Models with larger whiskers are more variable with stronger multi-decadal trends than models with smaller whiskers.

The variability of the whisker width among the models differs among the five metrics. The SAM (Figure 2a) shows the most variability among the models, with the width of the whiskers ranging from 3 hPa per 25 years to 10 hPa per 25 years (the mean and 2 sigma of the whisker length for the ensemble of models is 6 ± 3 hPa per 25 years). This indicates there is little agreement in the magnitude of the natural variability of the unforced system in SAM among the CMIP5 models. The jet location variability, U_{lat} (Figure 2b) and τ_{lat} (Figure 2c) also differs across the various models, but the differences are not as pronounced as in the SAM (whisker width is 2 ± 0.75 degrees per 25 years). There is even less variability between the models in jet magnitude. For the 850mb winds (Figure 2d) the whisker extent is $0.75 \pm 0.25 \text{ ms}^{-1}$ per 25 years, while for magnitude of the surface wind-stress (Figure 2e) it is approximately $0.015 \pm 0.005 \text{ Pa}$ per 25 years.

To better understand how these metrics compare to each other, we compare the linear correlations of each of the jet metrics with the SAM (Figure 3). The highest correlations occur between the SAM and the jet latitude metrics, with average R^2 values of 0.7 for both

2.3. RESULTS & DISCUSSION

TABLE 2.2: Probability of obtaining averaged reanalysis trend by only natural variability (first three columns) and natural variability + historical multi-model ensemble trend (second three columns).

Model	Natural Variability			Nat. Variability + Hist. Ensemble		
	SAM	U_{loc}	U_{max}	SAM	U_{loc}	U_{max}
CanESM2	5.98%	0.09%	0.03%	35.4%	9.77%	1.77 %
CNRM CM5	4.18 %	0.21%	0.28%	34.2%	6.45%	6.71 %
GFDL ESM2M	5.41%	1.05%	0.71%	32.1%	7.32%	6.92 %
IPSL CM5a LR	17.24%	2.79%	0.31%	39.5%	13.0%	5.54%
IPSL CM5a MR	9.29%	1.84 %	0.30%	33.0%	7.31%	4.70%
IPSL CM5b LR	16.3%	3.70 %	1.49%	39.8 %	15.3%	9.56%
MIROC ESM	5.69%	0.078%	0.032%	37.8%	3.80%	2.36 %
MIROC ESM CHEM	10.24%	0.52%	0.044%	34.4%	7.27%	1.78%
MIROC5	1.18%	0.005%	0.36%	26.7%	2.13%	3.65 %
MPI ESM LR	8.40%	1.70%	0.81%	34.8 %	10.4%	6.67%
MPI ESM MR	9.50%	1.81%	0.71%	40.3%	12.3%	7.61%
MRI CGCM3	5.14%	0.27%	0.93%	37.0%	7.24%	9.33%
NOR ESM1m M	3.98 %	0.09 %	0.05%	32.6%	5.30%	1.70 %
NOR ESM1m ME	3.63%	0.09%	0.04%	33.3%	4.46%	2.98 %

*Bolded values indicate a probability of 5% or higher.

τ_{lat} and U_{lat} . The correlations between the SAM and jet magnitude metrics are significantly lower with average R^2 values at 0.5, with the R^2 values for correlations of SAM with τ_{max} always being greater than that of SAM with U_{max} .

The comparison of magnitude of natural decadal variability of the different metrics and correlation between the metrics shows our first key result: The SAM, jet location and jet magnitude metrics are not interchangable.

2.3.2 Observed trends

With a description of the natural variability from the piControl run for each model, we now compare the observed reanalysis trends to the modeled natural variability to examine if the observed trend is forced or natural. In each panel in Figure 2.2, the dashed horizontal lines show the magnitude of the observed reanalysis trends. As expected from the above analysis there are differences among the different metrics.

The observed SAM trend observations lie just within the whiskers for most of the models, indicating the observed trends lie within the model natural variability. To quan-

2.3. RESULTS & DISCUSSION

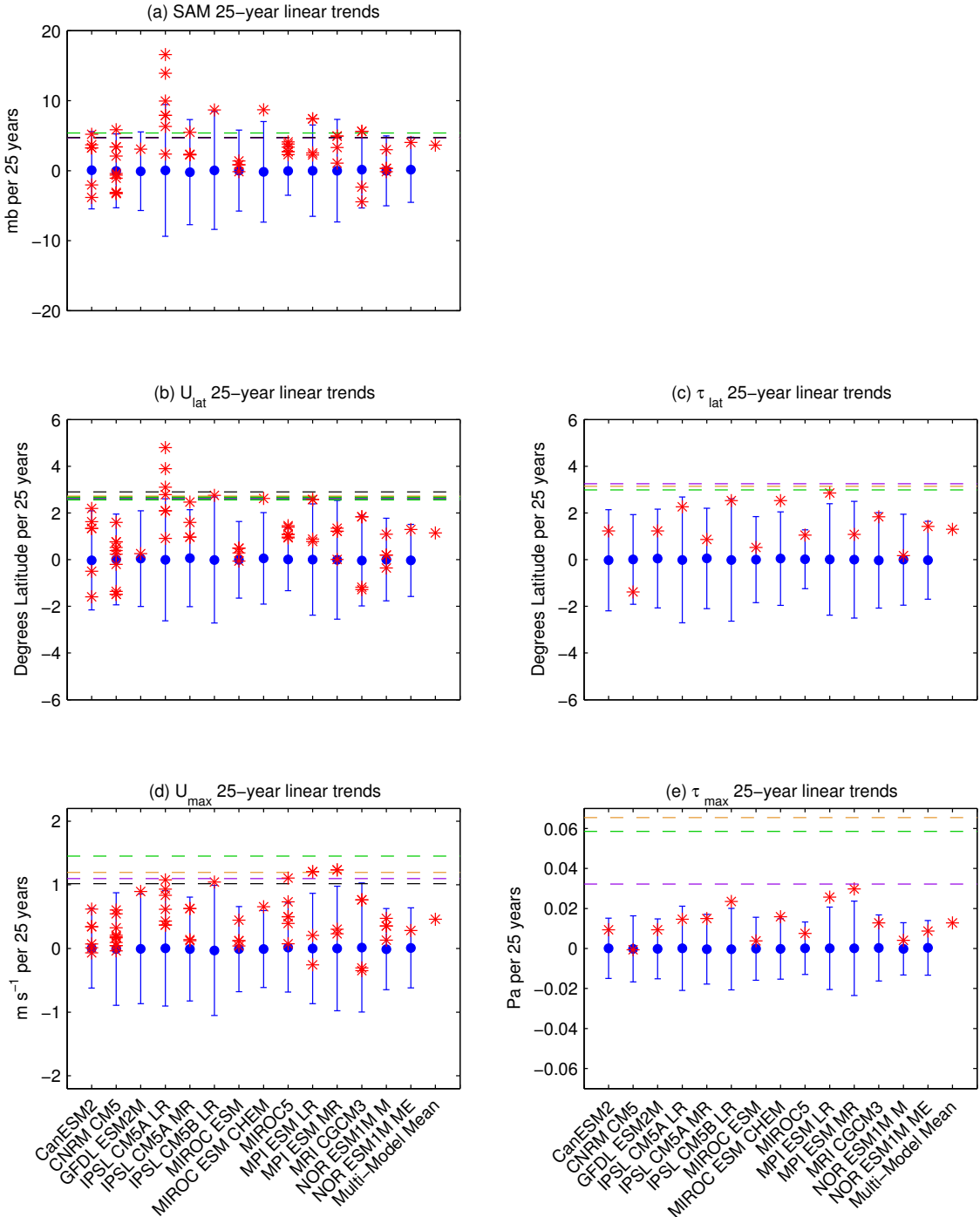


FIGURE 2.2: Natural variability, historical trends and observations for (a) SAM, (b) 850mb jet latitude, (c) wind-stress jet latitude, (d) 850mb jet magnitude, and (e) wind-stress jet magnitude. Blue circles show the mean of the piControl 25-year linear trends indicating model drift. Whisker length is 2 standard deviations. Red points show the historical run trends for each ensemble member. Horizontal dashed lines indicate the absolute value of the observed trends: NCEP R1 (green), NCEP R2 (orange), ERA-Int (purple), and JRA-55 (black).

2.3. RESULTS & DISCUSSION

tify this further, the probability of each model randomly obtaining a trend with the magnitude of the average reanalysis SAM trend or larger is shown in table 2 (column 1). 10 of the 14 models have a probability of 5% or greater, and thus there is a significant (at the 5% level) probability of obtaining the observed 25-year trend in the piControl simulations by chance alone. In other words, the observed trend over the period 1980-2004 in the SAM lies just within the edge of natural variability as described by these models. This result also holds for the period 1980-2014 (not shown).

The observed τ_{lat} and U_{lat} trends are just outside the model's natural decadal variability (Figure 2b and c). If we calculate the probability of each model obtaining the observed average reanalysis U_{lat} trend (table 2, column 2), then we see that no models have a probability of 5% or greater; however, 6 of the 14 have greater than a 1% probability. Thus, there is not a significant (at the 5% level) probability of obtaining the observed trend using natural variability alone.

In contrast, the observed trends in τ_{max} and U_{max} are both outside the natural variability as described by the models (Figure 2d and e). The probability of obtaining the average reanalysis U_{max} trend in all but one of the piControl models is less than 1% (table 2, column 3) and therefore there is not a significant (at the 1% level) probability of the natural variability reproducing the observed trend. The probabilities of the piControl τ_{max} and τ_{lat} obtaining the observed trends are not shown in table 2, but are consistent with the U_{max} and U_{lat} probabilities.

The above shows that the observed trends in the SAM largely lie at the edge of natural multi-decadal variability of the piControl model runs. However, this does not necessarily mean that the observed trends are not forced by anthropogenic activities, merely that the observations can contain a large component of natural variability in the SAM. The observed trend in the jet location and magnitude, however, is outside the variability of most models piControl runs. This does suggest an external force driving the jet to strengthen

2.3. RESULTS & DISCUSSION

and shift over this 25-year period.

2.3.3 *Model historical trends*

We now examine the model historical runs to understand how the modeled trends compare to the modeled natural variability and to compare the modeled trends with the observed trends. The red asterisks in Figure 2 represent the 25-year trend for each historical run (the number of historical runs varies among the models).

There is considerable variability amongst the models in the magnitude of the trends, but for all five metrics the vast majority of the simulated historical trends are of the same sign (increase in SAM, poleward shift and strengthening of the jet). This consistency in sign indicates that external (anthropogenic) forcing is causing at least part of the trend. However, the magnitude of the historical trends are almost all within the natural multi-decadal variability of the corresponding model (i.e. within the whiskers). Thus while the response in the models between 1980 and 2004 is due (at least in part) to forcing, the response does not overwhelm the natural variability.

For the SAM, the magnitude of the individual historical ensemble member trends are largely within the estimated natural variability and highly variable, with some ensemble members having trends of the opposite sign to the observations (dashed horizontal lines). Because the observed trends are generally within the natural decadal variability of the models a close agreement between individual historical ensemble members and observed trends would not be expected due to the high component of natural variability. Most of the ensemble members have positive trends and the magnitude of the multi-model ensemble mean historical trend is similar to the observations. This further suggests an anthropogenic forcing pushing the SAM towards positive phase.

The same comparison for jet location and magnitude yields different results. The observed trends in the jet metrics are outside the natural variability of the models, and

2.4. CONCLUSIONS

generally larger than the modeled historical trends (especially for the magnitude of the wind stress). A possible cause for this is that the observed trends are due to anthropogenic forcing that is not well represented (or under represented) in the models. However, another possibility is that there are issues with the reanalyses and the reanalyses are overestimating the real trend. This may especially be the case for the NCEP reanalyses, where the wind stress trends are significantly outside the model natural variability but the 850 hPa winds are just outside the model natural variability.

If we consider the observed trends to be a combination of natural variability and external forcing, and if we use the ensemble-mean historical trend as a representation of the forced response, we can better capture the observed trend. The last 3 columns in table 2 show the probability of obtaining the mean reanalysis trend from a combination of each model's natural variability and the multi-model ensemble mean historical trend (results for τ_{lat} and τ_{max} are not shown, but are consistent with U_{lat} and U_{max}). The probabilities for each metric are substantially greater, indicating that there is a significant probability, in most models, that the observed trends are due to this combination of natural variability and anthropogenic forcing. This does not exclude the possibility that the models are systematically biased low, or that the reanalyses are biased high, but it suggests that the mismatch is smaller than might be suggested from previous work [?].

2.4 Conclusions

Changes in the SAM are often linked with concurrent changes in the SH westerly jet magnitude and location [Hall & Visbeck, 2002]. Additionally, observational studies have shown recent trends in these diagnostics and attribute them to a combination of ozone depletion and greenhouse gas induced warming [?]. By comparing CMIP5 models piControl and historical runs with reanalysis observations, we have shown that there are significant differences in the observed and modeled trends of the SAM from those in the jet. Hence, the

2.4. CONCLUSIONS

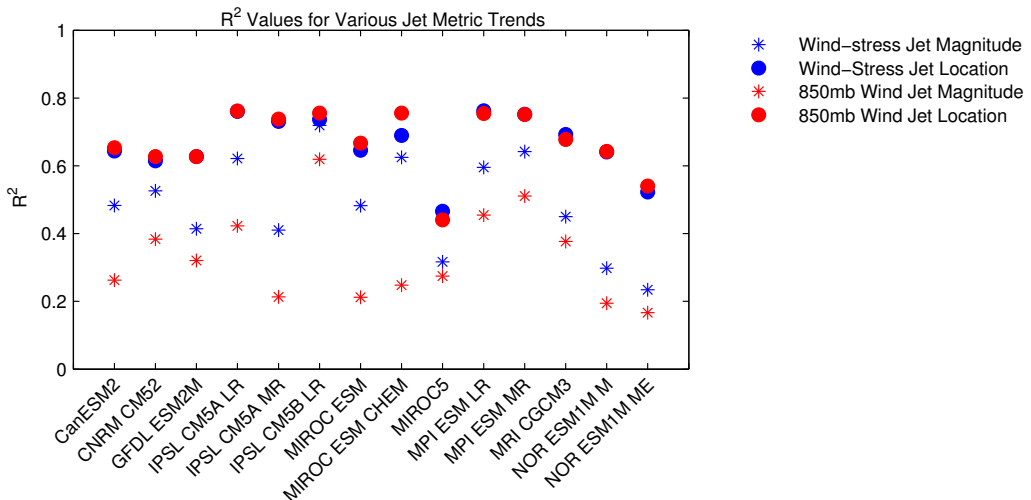


FIGURE 2.3: Correlation coefficient squared for correlation of the 25-year linear trends in wind-stress jet location, wind-stress jet magnitude, 850mb jet location, and 850mb jet magnitude with the 25-year trends in SAM for each model.

SAM and jet metrics cannot be used interchangeably.

Examining the natural variability of the SAM using CMIP5 preindustrial control runs has led to the conclusion that the observed trend is not decisively outside the natural variability as simulated by the CMIP5 models. While the modeled natural variability in SAM is quite large, the positive bias of the model historical trends suggest influence of an external forcing. The failure of individual historical models to simulate the magnitude of the observed historical trend could be due to the natural variability and not deficiencies in the simulations.

In contrast, the observed trends in jet location and magnitude are outside the natural variability of the models. The historical model runs also seem to underestimate the magnitude of these trends, especially in jet magnitude. Combining the natural variability and historical trend brings the models closer to capturing the observed trends in jet location and magnitude, but this does not eliminate the possibility that the model trends are biased low or the reanalyses are biased high.

Changes in the SAM and SH westerly jet have been linked with significant changes in

2.4. CONCLUSIONS

ocean circulation, ocean heat and carbon uptake [?], and Antarctic sea-ice extent [?]. We suggest that changes in SAM and jet latitude may behave differently than changes in jet magnitude and thus may have independent effects on the Southern Ocean and Antarctic climate. Understanding how these atmospheric variables interact with each other will be critical for predicting the future evolution of ocean circulation and the earth system.

CHAPTER 3

Ocean heat and carbon variability

The work contained in this chapter is based upon ?.

3.1 Introduction

The global ocean is an important component of the climate system. Holding far more heat and carbon than the atmosphere, it is an important sink for anthropogenic carbon and heat generated from greenhouse gas emissions. Observational estimates suggest that as of 1995, the ocean has been responsible for the uptake of approximately 100 Pg of anthropogenic carbon [Khatiwala *et al.*, 2012; Sabine *et al.*, 2004; Waugh *et al.*, 2006]. Temperature observations have also been used to estimate that the upper 2000 m of the ocean has been a sink for 15×10^{22} J of excess heat [Levitus *et al.*, 2009] between the years 1975–2005. Additionally, Frölicher *et al.* [2014a] demonstrated that in climate model simulations the Southern Ocean is an important region for oceanic uptake of anthropogenic carbon and heat. They estimate that 30% of anthropogenic carbon and 75% of anthropogenic heat that enters the ocean does so south of 30°S.

However, changes in the circulation due to both anthropogenic forcing and natu-

3.1. INTRODUCTION

ral variability may play an important role in heat and carbon uptake. Many studies have examined how changes in Southern Ocean circulation impact ocean carbon content [Sarmiento and Toggweiler, 1984; Sarmiento and Le Quere, 1996; Marinov *et al.*, 2008]. Between the 1980's to early 2000's, multiple studies linked an acceleration of the wind-driven Southern Ocean overturning with the resulting increase in upwelling of carbon-rich waters resulting in a decrease in the Southern Ocean CO₂ sink despite an increase in atmospheric CO₂ [Le Quere *et al.*, 2000; Lovenduski *et al.*, 2007; Lenton *et al.*, 2009]. More recently however, observational studies have suggested this weakening of the Southern Ocean carbon sink has reversed [Landschutzer *et al.*, 2015; Devries *et al.*, 2017], highlighting the importance of understanding natural variability. Finally, in many models, Weddell Sea deep convection has been determined to cause large fluctuations in ocean heat [Latif *et al.*, 2013; de Lavergne *et al.*, 2014] and carbon content [Bernardello *et al.*, 2014]. While significant effort has gone into understanding the net uptake of both heat and carbon, less research has focused on the natural fluctuations of heat and carbon content associated with longer (decadal-to-centennial) timescales of variability.

It is additionally important to examine heat and carbon variations together. A recent paper by Winton *et al.* [2013] showed that the impacts on heat and carbon uptake are different in response to changing ocean circulation. A change in ocean circulation has a larger influence on oceanic heat uptake than carbon uptake. This supports the results of Banks and Gregory [2006] and Xie and Vallis [2012] who show that temperature in the ocean does not in fact behave as a passive tracer.

While studies have focused on the forced response of oceanic heat and carbon and have demonstrated that heat and carbon have different storage and uptake patterns, we are unaware of any studies that have explored the un-forced co-variability of heat and carbon content. In this paper, we investigate natural variability of both heat and carbon content in multiple simulations of an Earth-system model. We examine the magnitude and frequency of the variability in global heat and carbon content in simulations with

3.2. METHODS

various mesoscale mixing parameter settings. We then look more closely at the regional and spatial patterns of variability and finally, we propose possible mechanisms that drive this variability. Varying the mesoscale mixing parameters allows us to test the sensitivity of the patterns of variability and the mechanisms driving this variability. This analysis aims to help understand the magnitude of natural variability and provide a context with which to view anthropogenic trends. Additionally it aids in the understanding of how carbon and heat vary with respect to each other.

Descriptions of the model used and quantities examined is found in section 4.3. Section 3.3 discusses the temporal and spatial variability in heat and carbon content. The mechanisms driving this variability are examined in section 3.4, and conclusions are in section 3.5.

3.2 Methods

3.2.1 *Model and Simulation Descriptions*

We use the GFDL ESM2Mc [Galbraith *et al.*, 2011], a coarse resolution configuration of the GFDL ESM2M [Dunne *et al.*, 2012]. The model has an atmospheric resolution of $3.875^\circ \times 3^\circ$ with 24 vertical levels. The ocean model is non-Boussinesq, using pressure as the vertical coordinate, and has a resolution of $3^\circ \times 1.5^\circ$ and 28 vertical levels. Despite its relatively coarse resolution, ESM2Mc has a realistic simulation of the Southern Annular Mode [Galbraith *et al.*, 2011], response of Southern Hemisphere winds to an ozone hole [Seviour *et al.*, 2017], and El Niño Southern Oscillation [Russell and Gnanadesikan, 2014]. The vertical tracer diffusion coefficient (K_v) value is set within the KPP module. The value increases with depth and buoyancy forcing. When the water column is statically unstable the value can exceed 4 m s^{-2} which implies an equilibration time of approximately 5 days even for a water column that is 4000 m deep. The oceanic model also has a coupled biogeochemical module referred to as the Biogeochemistry with Light Iron Nutrients and Gases (BLING)

3.2. METHODS

model [Galbraith *et al.*, 2010]. Although this module uses a highly parameterized biological cycle, it predicts patterns of carbon and oxygen change in response to global warming that are very similar to a more complex biogeochemistry simulation in ESM2M [Galbraith *et al.*, 2015].

Because of the coarse resolution, processes associated with oceanic eddies are parameterized. The mesoscale advection of tracers along isopycnals is parameterized using the Gent-McWilliams parameterization scheme [Gent and Mcwilliams, 2010]. The diffusion coefficient, A_{GM} , varies spatially depending on the meridional gradient of the vertical shear between 100 m – 2000 m. A default minimum and maximum value of A_{GM} is imposed at $200 \text{ m}^2\text{s}^{-1}$ and $1400 \text{ m}^2\text{s}^{-1}$ respectively. Additionally, the along-isopycnal diffusion (neutral diffusion) by mesoscale eddies is parameterized using a coordinate rotation method [Redi, 1982]. The neutral diffusion coefficient, A_{redi} , is set to a spatially constant value of $800 \text{ m}^2\text{s}^{-1}$ by default.

The model was initialized using the World Ocean Atlas present-day observations of temperature, salinity, and nutrients and was run for 1500 years with pre-industrial (1860) values of greenhouse gases and aerosols. An additional 500 years were simulated using the default value of A_{redi} ($800 \text{ m}^2\text{s}^{-1}$) and this simulation is referenced as the *control* simulation. At year 1500, the model was branched to produce two more 500-year simulations using different, constant values of $A_{redi} = 400$ and $2400 \text{ m}^2\text{s}^{-1}$. These runs are referred to as the *low eddy diffusion* and *high eddy diffusion* runs respectively. As discussed in Pradal and Gnanadesikan [2014] and Gnanadesikan *et al.* [2015], the value of A_{redi} varies significantly across modern climate models, which tend to use values lower than observational estimates [Ollitrault and Colin de Verdière, 2002]. The range of values used here is comparable to those seen in the CMIP5 model suite. One final 500-year simulation was conducted by branching the control run and changing the minimum value of the mesoscale eddy advection coefficient, A_{GM} , to be $600 \text{ m}^2\text{s}^{-1}$ while maintaining the default value of A_{redi} ($800 \text{ m}^2\text{s}^{-1}$). This is referred to at the *high eddy advection* simulation.

3.2. METHODS

Figure 3.1 shows the winter-time climatologies (JJA) for various Southern Hemisphere metrics with comparison to observations for all simulations. The Southern Ocean temperature (Figure 3.1 (a)) in the surface layer is biased warm for all simulations. Additionally, all simulations except the *high eddy diffusion* simulation have subsurface temperatures exceeding the observations. Similarly, the modeled surface salinity (Figure 3.1 (b)) is biased fresh for all simulations except the *high eddy diffusion* simulation. Figure 3.1 (c) shows the profile of density stratification strength ($\sigma_0 - \sigma_0^{1500m}$). The model simulations envelop the observational density stratification with the *high eddy advection* simulation having the strongest density stratification and the *high eddy diffusion* simulation having the weakest stratification. The comparison of the modeled Southern Hemisphere westerly wind stress with the ERA-Interim westerly wind stress is shown in Figure 3.1 (d). All the model simulations underestimate the strength of the wind stress south of 40°S and have an equatorward-biased peak in the wind stress. Finally comparison with the observational sea ice-extent is shown in Figure 3.1 (e). All simulations under estimate the sea ice extent in all months except the *high eddy advection* simulation which has accurate sea ice extent values in the austral spring.

The various A_{redi} simulations are discussed at length in *Pradal and Gnanadesikan [2014]* and *Gnanadesikan et al. [2015]*, which examine the mean climate response and sensitivity of anthropogenic carbon uptake to changing the A_{redi} parameter. Here instead, we use the various simulations to test the robustness of the mechanisms driving the co-variability of heat and carbon. Because the different simulations have varying Weddell Sea convective variability (similar to the spread in CMIP5 models, see below), we can see if convection alters the mechanisms driving the co-variability of heat and carbon in this model. Unlike the CMIP5 suite where differences in biological models, atmospheric radiation code, and sea ice formation contribute to intermodel spread, our simulations differ only in the mesoscale parameterizations to isolate the influence of Weddell Sea convection on the co-variability of heat and carbon content.

3.2. METHODS

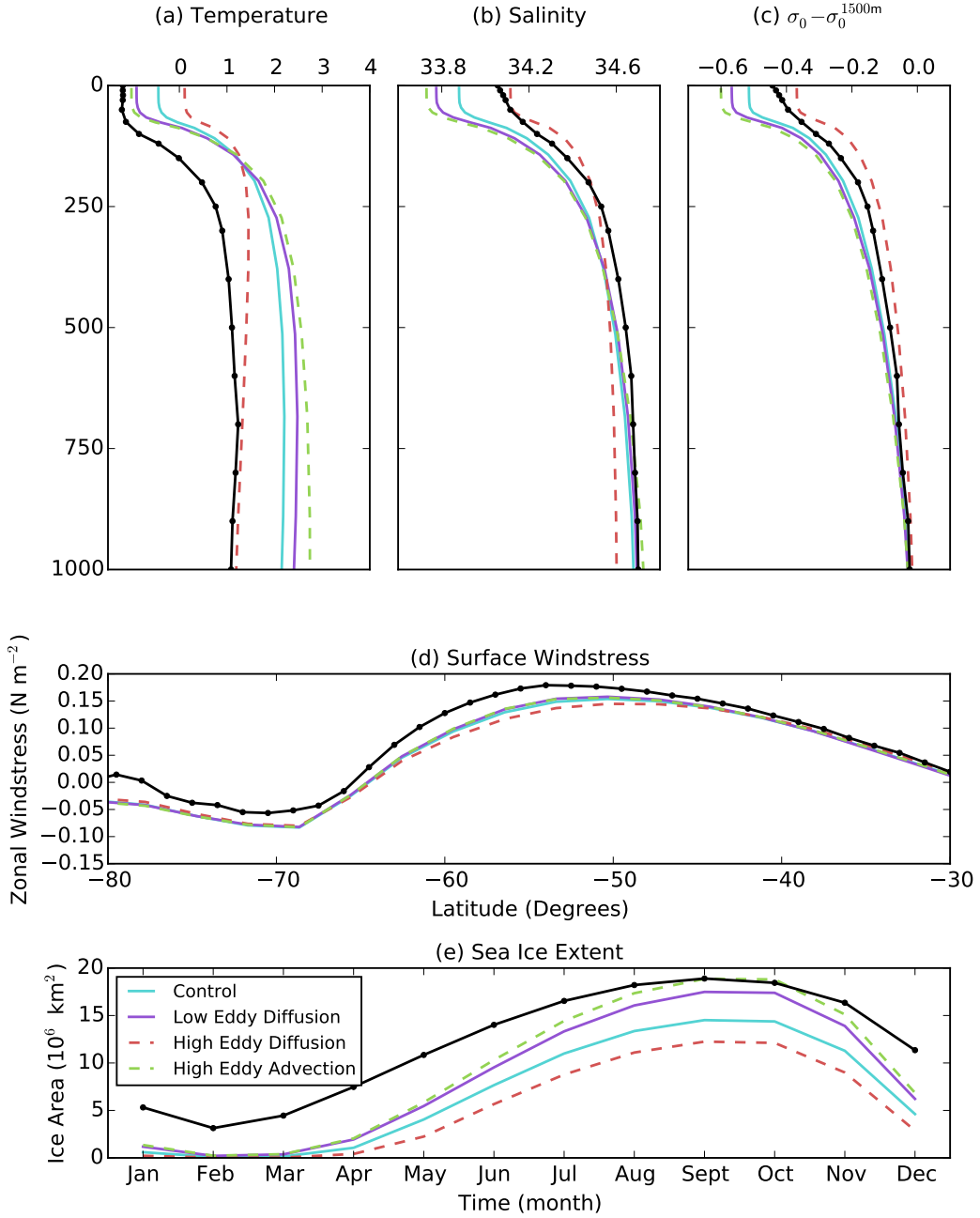


FIGURE 3.1: Comparison of control (blue), low eddy diffusion (purple), high eddy diffusion (red), and high eddy advection (green) simulations. JJA Southern Ocean (60–90°S) (a) temperature (b) salinity and (c) density stratification ($\sigma_0 - \sigma_0^{1500m}$). (d) JJA zonal surface wind stress and (e) Antarctic sea ice extent. Observational data for each metric is shown in black. Temperature, salinity, density stratification are estimates from the 2001 World Ocean Atlas 2001 dataset [Boyer *et al.*, 2002]. Surface wind stress are from ERA-Interim and averaged between 1979–2015. Sea extent is calculated using the National Snow and Ice Data Center Sea Ice Index [Fetterer *et al.*, 2016]

3.2.2 Heat and Carbon Content

Heat and carbon content are calculated globally and regionally. The oceanic heat content (H) is calculated using the subsurface potential temperature (θ), and integrated globally:

$$H_{global} = \sum_{k=0}^{bottom} \sum_{j=-90}^{90} \sum_{i=0}^{360} \rho c_p \theta \delta x_i \delta y_j \delta z_k \quad (3.1)$$

Similarly, carbon content is calculated using Dissolved Inorganic Carbon (DIC) concentration and integrated globally:

$$C_{global} = \sum_{k=0}^{bottom} \sum_{j=-90}^{90} \sum_{i=0}^{360} \rho [DIC] \delta x_i \delta y_j \delta z_k \quad (3.2)$$

Because the oceanic heat and carbon reservoirs are so large ($150,000 \times 10^{22}$ J and 37,000 PgC, respectively), and the natural variability relatively small ($\pm 3 \times 10^{22}$ J and ± 3 PgC, respectively), we express the variability as an anomaly from the climatological mean.

3.2.3 Surface Heat Flux

We determine the surface heat flux by vertically integrating the vertical diffusion term over the entire water column and subtracting the geothermal heat flux from the sea floor:

$$\sum_{k=0}^{bottom} \left(\rho_k c_p \left(\frac{\partial \theta}{\partial t} \right)_{vdiff} \right)_k \delta z_k - Q_{geo} = \\ Q_{SW} + Q_{LW} + Q_{latent} + Q_{sensible} = Q_{surface} \quad (3.3)$$

The advantage to defining the surface heat flux with this method, as opposed to the model-calculated surface heat flux, is that we can determine the heat lost to overlying sea ice in addition to the atmosphere as well as track heat sinks such as the melting of snow.

3.2. METHODS

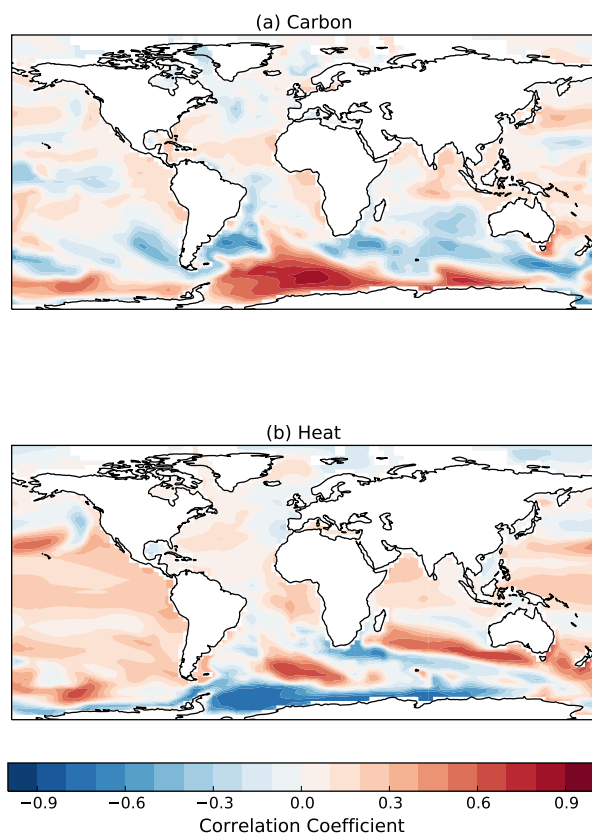


FIGURE 3.2: Correlation between (a) vertically integrated carbon content at each location and global carbon content and (b) vertically integrated heat content at each location and global heat content for the control simulation ($A_{\text{redi}} = 800 \text{ m s}^{-2}$).

3.2.4 Southern Ocean

As has been previously documented [*de Lavergne et al.*, 2014], ESM2Mc has a particularly active Southern Ocean. Deep convective events occur often in the Southern Ocean, and have a sizable impact on the climate system. *Cabre et al.* [2017] recently showed that Southern Ocean convective events in this model have an impact on the Southern Hemisphere surface temperatures, Hadley cell, and radiative balance. In light of the Southern Ocean influence in this model, we first assessed the contribution of Southern Ocean variability to global heat and carbon variability. Figure 3.2 shows the correlation between vertically integrated carbon (heat) content at each location with the global carbon (heat) content in the *control* simulation. This initial analysis suggests the importance of the Southern Ocean, and particularly the Weddell Sea on global heat and carbon variability and will be more thoroughly examined in section 3.3.

3.3 Temporal and Spatial Variations in Heat and Carbon Content

3.3.1 Weddell Sea Convection

In the mid-1970s, an anomalous opening in the sea ice in the Weddell Sea was observed [*Carsey, 1980*]. Named the Weddell Polynya, this large opening was observed for three consecutive austral winters: 1974–1976. The polynya was formed and maintained by vigorous convective mixing where the upward flux of deep and relatively warm waters provided enough energy to melt the above sea ice [*Gordon, 1982; Martinson et al., 1981*]. This heat loss at the surface resulted in subsurface cooling deep into the water column, depleting the subsurface heat reservoir.

While a large feature like the Weddell Polynya has not been observed since and is considered to be a rare event, these polynya events can be quite common in climate models. A recent paper by *de Lavergne et al.* [2014] quantifies these convective events in CMIP5 model preindustrial control simulations and shows the spread across models. They find

3.3. TEMPORAL AND SPATIAL VARIATIONS IN HEAT AND CARBON CONTENT

that some CMIP5 models have very little convection, while others have constant deep convection, with most models lying somewhere in between.

Changing the mesoscale eddy parameterization in our model suite has a large impact on the Weddell Sea deep convection. Figure 3.3 shows the annually-averaged subsurface temperature as a function of time (colored contours) and the annual mixed layer depth (black line) averaged over the Weddell Sea (60–80°S, 60°W–0). The downward spikes in mixed layer depth, and the concurrent decline in subsurface temperature indicate the occurrence of a deep convective event. The simulations range from no convection in the *high eddy advection simulation* (Figure 3.3 (d)), to constantly convecting in the *high eddy diffusion simulation* (Figure 3.3 (c)), with the *control* and *low eddy diffusion* cases oscillating between convective and non-convective periods (Figure 3.3 (a) and (b)).

When the neutral diffusion coefficient (A_{redi}) is increased as in the *high eddy diffusion* simulation, the along-isopycnal diffusive mixing is increased. In the Southern Ocean where the isopycnals slope up to the surface and the subsurface water is warmer than the surface ocean, this increased along-isopycnal diffusion acts to decrease the vertical gradient in temperature and salinity (also shown in Figure 3.1 (a) - (c)). This results in a lower subsurface temperature, a weaker density contrast between deep and surface waters, less subsurface heat build-up, and no large convective ‘events’ (Figure 3.3 (c)). Alternatively, a lower neutral diffusion coefficient as in the *control* and *low eddy diffusion* simulations does the opposite: the along-isopycnal diffusive mixing is decreased and subsurface heat is able to build up until a deep convective event occurs (Figure 3.3 (a) and (b)).

Changing the eddy advection coefficient (A_{GM}) on the other hand impacts the slope of the isopycnal surfaces. As shown in Gent *et al.* [1995], increasing A_{GM} acts to flatten the isopycnal surfaces and reduce vertical exchange. In the Southern Ocean where the isopycnals slope up to the surface, and the A_{GM} value is usually small, increasing the minimum value of A_{GM} thus reinforces the vertical density gradient. The result is a build-up

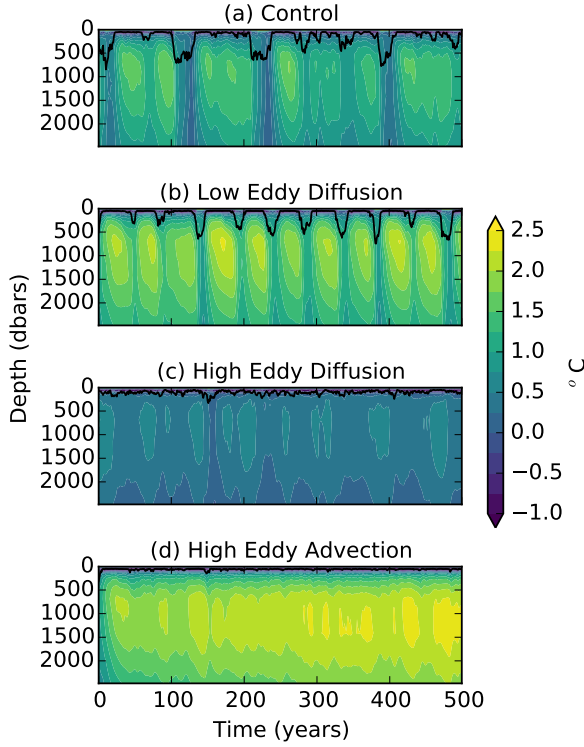


FIGURE 3.3: Annually averaged subsurface temperature (color contours) and mixed layer depth (solid black line) averaged over Weddell Sea for (a) Control simulation ($A_{\text{redi}} = 800 \text{ m s}^{-2}$), (b) Low Eddy Diffusion simulation ($A_{\text{redi}} = 400 \text{ m s}^{-2}$), (c) High Eddy Diffusion simulation ($A_{\text{redi}} = 2400 \text{ m s}^{-2}$), and (d) High Eddy Advection simulation ($GM_{\text{min}} = 600 \text{ m s}^{-2}$).

of subsurface heat that continues to grow throughout the *high eddy advection* simulation. The reinforced density gradient is strong enough to suppress deep convection throughout the 500-year simulation (Figure 3.3 (d)).

It is important to note that while the existence of subsurface heat build-up is known to be important for the existence of deep convective events, it is not yet known what mechanism initiates deep convection in the model or sets the timescales for convective variability. We have found, however, that by changing these parameterizations, we are able to span the range of convective variability seen in CMIP5 models as shown in *de Lavergne et al. [2014]* without the additional complications introduced by different representations of atmospheric processes and biological cycling. In this paper we will use these different convective states of the model to identify the impact convective variability has on both carbon and heat in the Southern Ocean and globally.

3.3.2 Global Heat and Carbon Variability

We first aim to understand the variability in global oceanic heat and carbon content in the *control* simulation. The time-series of global carbon and heat content anomaly is shown in Figure 3.4 (a) and (b). Both quantities show strong multi-decadal-scale variability, undergoing strong fluctuations roughly every 50 years. The magnitude of global carbon variability is about ± 3 PgC which accounts for only approximately 3% of the estimated anthropogenic uptake of carbon over the past few decades [Khatiwala *et al.*, 2012; Sabine *et al.*, 2004; Waugh *et al.*, 2006]. The variability in global heat content on the other hand is about $\pm 3 \times 10^{22}$ J. This is a much larger percentage (20%) of the estimated uptake of anthropogenic in heat recent decades [Levitus *et al.*, 2009]. Figure 3.4 (c) shows the time-series of Weddell Sea (WS) subsurface temperature (averaged between 1500 m and 2500 m). This quantity has been shown to be a good proxy for WS deep convection since the subsurface temperature is significantly decreased during convective events [Bernardello *et al.*, 2014]. Comparing the time-series of the WS subsurface temperature to those of global heat and carbon anomalies, it is apparent that there is a strong relationship. In the control simulation, the WS subsurface temperature explains 61% and 35% (r^2) of the variance in global heat content and carbon content respectively (Table 3.1), with the strongest correlation occurring at time lag = 0. The correlation between WS subsurface temperature and global heat and carbon content is also high for the *low eddy diffusion* simulation, while the relationship is less strong (yet significant) for the *high eddy diffusion* and *high eddy advection* simulations (Table 3.1). These results suggest that WS convection is closely tied to the global heat and carbon content.

The global heat and carbon content anomaly time-series for all simulations is shown in Figure 3.5. The magnitude and frequency of heat and carbon content variability changes substantially across the different simulations. Comparing the time-series of global carbon content and heat content anomalies in the control simulation we find that they are anti-

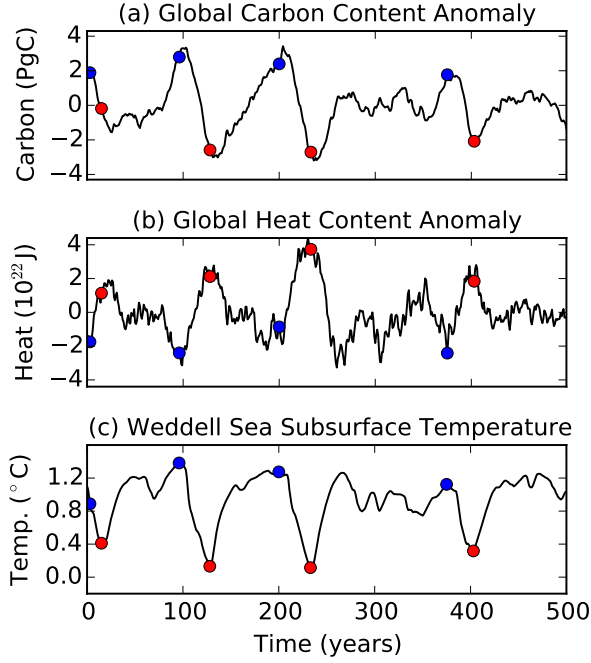


FIGURE 3.4: Carbon content anomaly, heat content anomaly and Weddell Sea subsurface temperature (averaged between 1500–2000 m, 0°–60°W, 60°–80°S) for control simulation. Blue circles indicate beginning of convection and red circles indicate end of convection defined using four strongest local maxima and minima in Weddell Sea Subsurface Temperature.

correlated ($r = -0.629$, Figure 3.6). Given that in this model, the global heat and carbon are primarily driven by Southern Ocean variability and Southern Ocean convection acts to deplete the Southern Ocean of both carbon and heat content, we would expect that global heat and carbon content should vary together. Therefore it is surprising that the two quantities are so strongly negatively correlated.

This anti-correlation relationship between global heat and carbon content is consistent in the additional simulations as well (Figure 3.5). Figure 3.6 shows the Pearson correlation coefficient between global heat and carbon content for each simulation. All of the simulations have a statistically significant negative correlation between global heat and carbon exceeding -0.3. The two simulations which oscillate between convective and non-convective periods (*control* and *low eddy diffusion*) have stronger correlations at or exceeding -0.5. The fact that significant anti-correlation is found for all simulations suggests that the mechanisms causing this anti-correlation in global heat and carbon content are

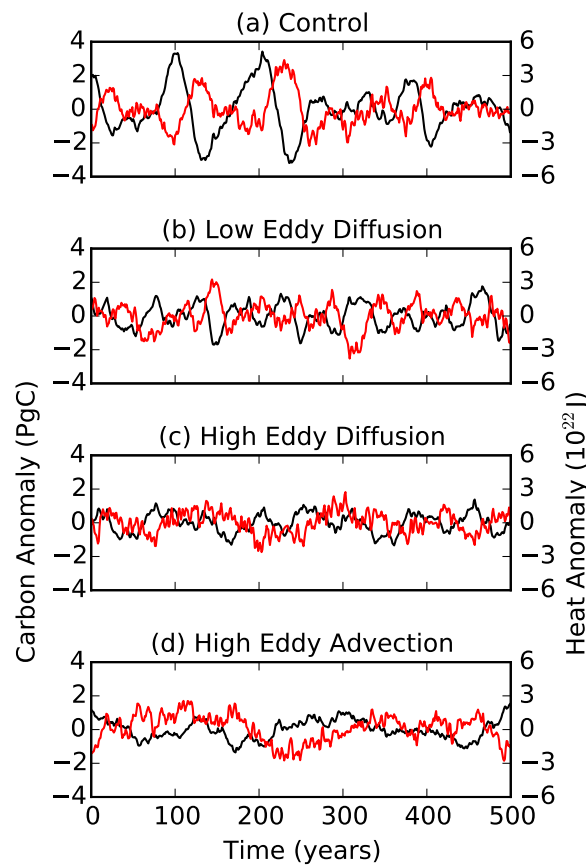


FIGURE 3.5: Globally integrated carbon content anomaly (black) and heat content anomaly (red) for (a) Control simulation ($A_{\text{redi}} = 800 \text{ m s}^{-2}$), (b) Low Eddy Diffusion simulation ($A_{\text{redi}} = 400 \text{ m s}^{-2}$), (c) High Eddy Diffusion simulation ($A_{\text{redi}} = 2400 \text{ m s}^{-2}$), and (d) High Eddy Advection simulation ($GM_{\min} = 600 \text{ m s}^{-2}$).

3.3. TEMPORAL AND SPATIAL VARIATIONS IN HEAT AND CARBON CONTENT

TABLE 3.1: Relationship between Weddell Sea subsurface temperature and global carbon and heat content anomalies. All correlations are statistically significant from 0 ($p = 0.005$).

Simulation	Carbon Content	Heat Content
	<i>Correlations (r)</i>	
Control	0.59	-0.79
Low Aredi	0.61	-0.56
High Aredi	0.49	-0.20
High GM_{\min} min	0.12	-0.24

not strongly dependent on the convective state in the WS.

In light of these results, we find it helpful to divide these simulations up into two classes: the *low mixing simulations* which oscillate between convective and non-convective periods (control and low eddy diffusion) and the *high mixing simulations* simulations which do not (high eddy diffusion and high eddy advection). The low mixing simulations are characterized by a build-up and subsequent release of abyssal heat content in the Southern Ocean (Figure 3.3). These two simulations also have very strong oscillations in the global heat and carbon content, closely linked to the WS convection. The high mixing simulations on the other hand do not show this oscillation between subsurface build-up and release in the Southern Ocean, but rather either constant depletion in subsurface temperature in the *high eddy diffusion* (Figure 3.3 (c)) or a constant build-up of subsurface temperature in the *high eddy advection* (Figure 3.3 (d)). The lack of these oscillating convective states results in smaller global heat and carbon variability (Figure 3.5), and a weaker relationship (although significant) between the WS and the global heat and carbon content.

To understand why the global heat and carbon are strongly anti-correlated, next we look at the regional relationships between heat and carbon content.

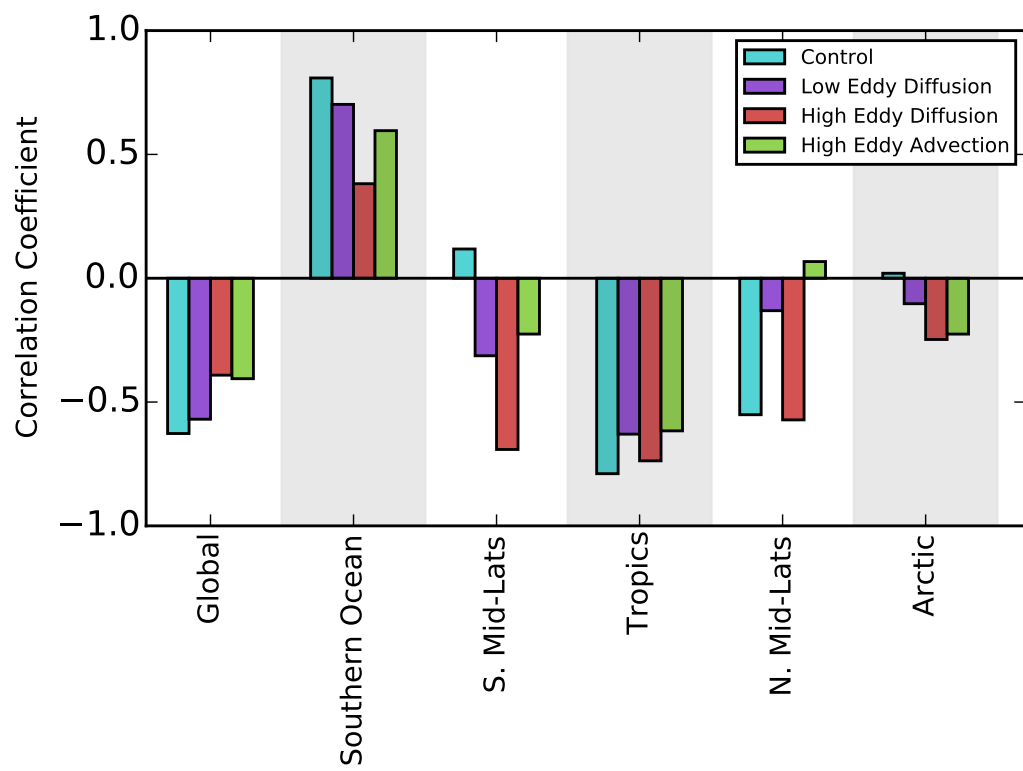


FIGURE 3.6: Pearson correlation coefficients for integrated carbon content anomaly versus integrated heat content anomaly for each region.

3.3.3 *Regional Heat and Carbon Variability*

To diagnose which regions significantly contribute to the observed variability in global heat and carbon content, we break the global ocean into zonal bands: the Southern Ocean (90°S – 55°S), the southern mid-latitudes (55°S – 20°S), tropics (20°S – 20°N), the northern mid-latitudes (20°N – 60°N), and the Arctic (60°N – 90°N). These divisions were defined by the zonal average of the zero wind-stress curl in order to isolate the dynamical regions (not shown). The correlation coefficients between heat and carbon content in each of these regions are also shown in Figure 3.6. The correlation coefficients give a sense of what remains consistent across the simulations even with the different convective states. The Southern Ocean has a strong positive correlation between heat and carbon for all the simulations. Additionally, in the tropics there is a strong negative correlation between heat and carbon for all the simulations. This result suggests that the negative correlation in the tropics is key to understanding the negative correlation between heat and carbon seen globally.

To get a better sense of which regions dominate the variability, we decompose the global heat and carbon regionally by regressing the regional inventories of heat and carbon against the global inventories of heat and carbon. We first consider heat content in the *control* simulation (Figure 3.7 (a), red dots). The regression highlights the importance of three regions in contributing to the global heat content signal: the Southern Ocean, southern mid-latitudes, and tropics. The Southern Ocean regression coefficient has a magnitude similar to the southern mid-latitudes and tropics, but the opposite sign. This indicates that the variability in Southern Ocean heat content is being compensated by similar magnitude variability in heat content in both the southern mid-latitudes and tropics.

The picture is nearly identical in the *low eddy diffusion* simulation (which also undergoes oscillations between convective and non-convective states). The Southern Ocean heat content variability is compensated by similar magnitude variability in both the southern

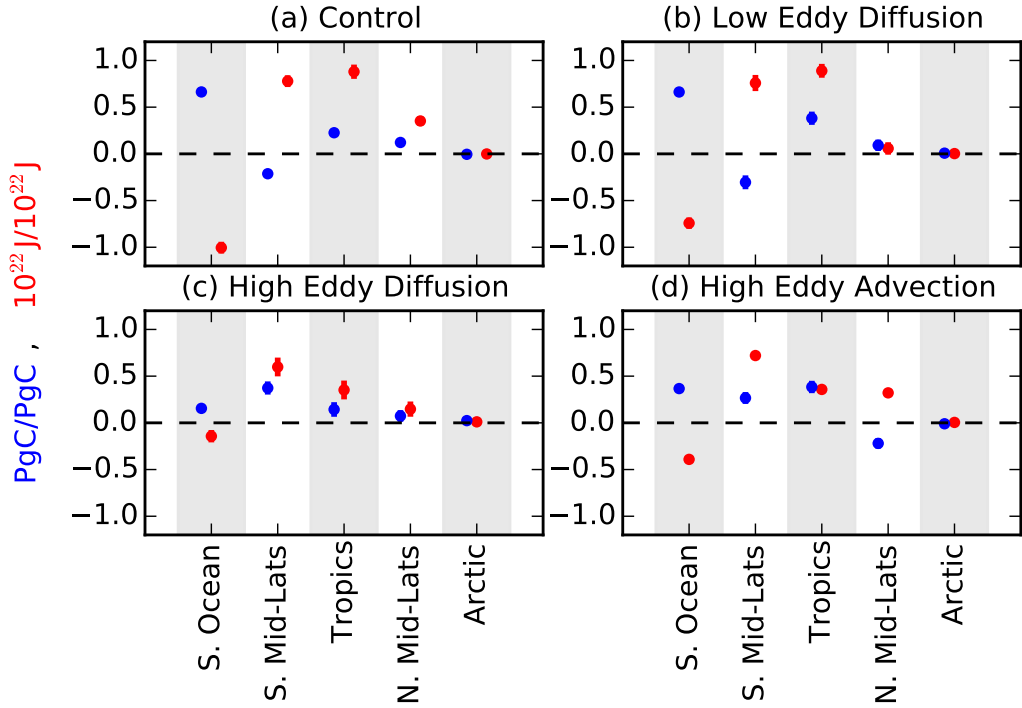


FIGURE 3.7: Linear regression of each region's carbon content against global carbon content (blue) and each regions heat content against global heat content (red). Linear regression 95% confidence interval is shown, but too small to be discerned.

mid-latitudes and tropics (Figure 3.7 (b)). However, the *high mixing* simulations are less clear. The regional heat content is dominated by the southern mid-latitudes with weak compensation between the Southern Ocean and tropics (Figure 3.7 (c) and (d)).

The linear regression of regional carbon content (Figure 3.7, blue dots), however, suggests that the Southern Ocean carbon content variability contributes most towards the global carbon content variability for all simulations. For the *low mixing simulations*, there appears to be a compensation between the southern mid-latitude and tropical carbon content variability. This compensation in regional variability is not seen in the *high mixing simulations* where the regression coefficients are both positive for these two regions. Regardless of these differences, the Southern Ocean is the region with the largest regression coefficient for all simulations.

The time series of the regional variability for heat and carbon content compared to

3.3. TEMPORAL AND SPATIAL VARIATIONS IN HEAT AND CARBON CONTENT

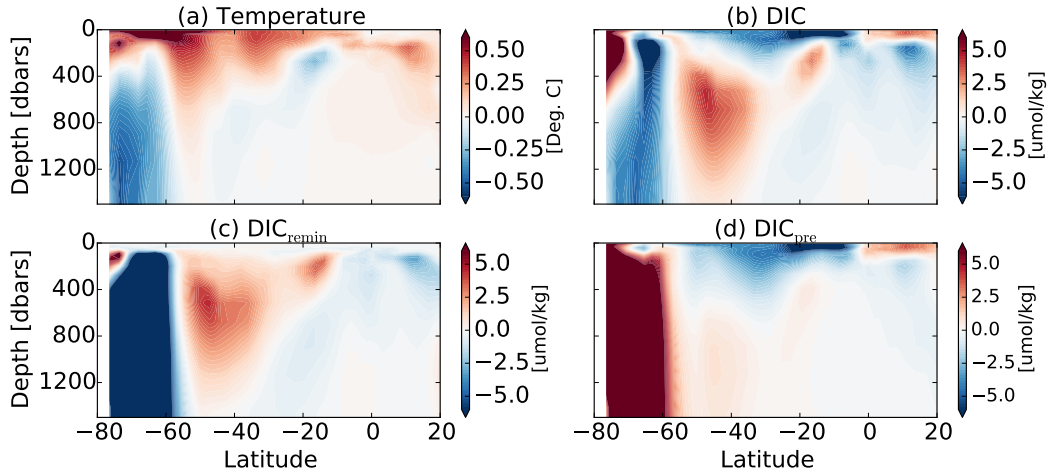


FIGURE 3.8: Subsurface (a) potential temperature, (b) DIC, (c) remineralized DIC, and (d) preformed DIC for convective year composite from control simulation. Only the surface ocean is shown to highlight the strongest-magnitude features.

the global heat and carbon content are shown in the supplemental information as an additional way to visualize the offsetting variations in different regions.

This relationship between WS deep convection and Southern Hemisphere surface warming is consistent with *Bernardello et al.* [2014] and *Cabre et al.* [2017]. Both papers use the same GFDL model shown here in the control configuration to assess the impact of convection on the climate system and both sets of analysis show similar Southern Hemisphere surface warming in response to a convective event. Specifically, *Cabre et al.* [2017] show that during these winter time convective events, substantial warming occurs in the Southern Ocean, increasing sea surface temperatures, decreasing sea ice and low clouds, and increasing solar radiation absorption. The result is a substantial warming of the Southern Hemisphere surface ocean and atmosphere. This atmospheric warming propagates to the rest of the atmosphere almost instantaneously, changing the meridional temperature gradient and altering the strength of the Hadley Cell in both hemispheres. For a more detailed look at the teleconnections between the Southern Ocean convection and tropical SST increases, we refer the reader to *Cabre et al.* [2017].

3.4 Mechanisms Driving Variability

In order to understand why global heat and carbon content are anti-correlated we look more in depth at the mechanisms driving the regional variability of these quantities.

3.4.1 Heat Content Variability

We first examine the variability of heat content. As shown for the *control* simulation subsurface temperature in Figure 3.8 (a), convection acts to deplete the Southern Ocean of subsurface heat, and increase the surface heat content in the southern mid-latitudes and tropics. These processes are more explicitly shown in Figure 3.9. Periods of convection (highlighted in grey) are consistent with deepening of the mixed layer (black line), a depletion of subsurface Southern Ocean temperature (green line), an increase in Southern Ocean heat flux into the atmosphere (negative out of ocean – red line), and an increase in southern mid-latitude and tropical SST (blue line). These processes are consistent in the *low eddy diffusion* simulation which also oscillates between convective and non-convective periods (not shown).

This relationship between WS deep convection and Southern Hemisphere surface warming is consistent with *Bernardello et al.* [2014] and *Cabre et al.* [2017]. Both papers use the same GFDL model shown here to assess the impact of convection on the climate system and both sets of analysis show similar Southern Hemisphere surface warming in response to a convective event. Specifically, *Cabre et al.* [2017] show that during these winter time convective events, substantial warming occurs in the Southern Ocean, increasing sea surface temperatures, decreasing sea ice and low clouds, and increasing solar radiation absorption. The result is a substantial warming of the Southern Hemisphere surface ocean and atmosphere. This atmospheric warming propagates to the rest of the atmosphere almost instantaneously, changing the meridional temperature gradient and altering the strength of the Hadley Cell in both hemispheres. For a more detailed look at the telecon-

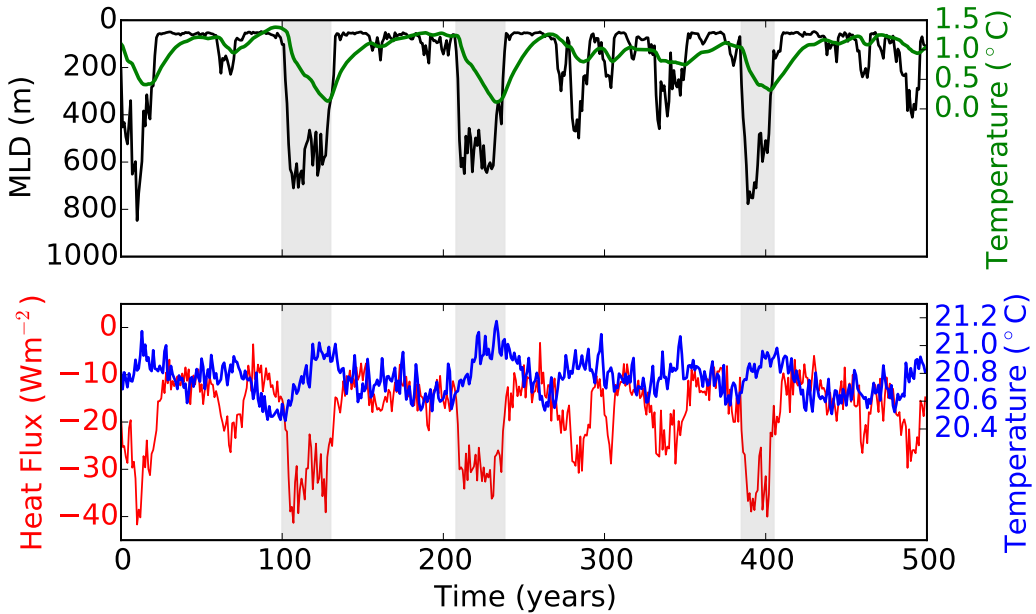


FIGURE 3.9: Top: Weddell Sea subsurface temperature as in Figure 3.4 (green) and Weddell Sea mixed layer depth (black). Bottom: Southern Ocean surface heat flux where positive indicates into the ocean (red), Southern Hemisphere SST averaged between 0° – 55°S (blue) for the control simulation.

nnections between the Southern Ocean convection and tropical SST increases, we refer the reader to *Cabré et al. [2017]*.

In this paper we show that the impact of this surface warming in the southern mid-latitudes and tropics is strong enough to counteract the depletion of subsurface heat in the Southern Ocean, resulting in a global increase in heat content after WS convection.

3.4.2 Carbon Content Variability

Next we examine the regional mechanisms driving variability in carbon content in order to understand the anti-correlation between global heat and carbon content. Examining the *control* simulation (Figure 3.8 (b)), we see that during convection there is a strong subsurface depletion of DIC in the Southern Ocean, an increase in subsurface DIC in the southern mid-latitudes, and a further depletion of surface-layer DIC in the southern mid-latitudes to equator. To understand these spatial patterns, we break the DIC up into two

3.4. MECHANISMS DRIVING VARIABILITY

components:

$$DIC = DIC_{pre} + DIC_{remin} \quad (3.4)$$

where the preformed component (DIC_{pre}) is the DIC concentration of the water at the ocean surface and the remineralized component (DIC_{remin}) is the carbon concentration due to biological accumulation. DIC_{pre} is set equal to DIC in the mixed layer and is advected and mixed into the ocean interior with biological sources and sinks set to zero. Thus by definition, DIC_{remin} is zero within the mixed layer and represents the component of DIC in the interior that is due to biological sources and sinks.

When breaking the DIC down into its two components, we see that in the Southern Ocean there is a very strong depletion of subsurface remineralized carbon and a strong increase in preformed carbon (Figure 3.8 (c) and (d)). This signal is consistent with deep convective mixing. The increase in subsurface DIC_{pre} occurs from mixing relatively high surface DIC_{pre} down into the subsurface and the decrease in DIC_{remin} occurs from mixing relatively high DIC_{remin} from the subsurface to the surface layer. Mixing these high DIC waters from the abyssal Southern Ocean to the surface results in outgassing of CO₂ to the atmosphere (not shown) and the net result is a reduction in subsurface DIC.

The depletion in surface DIC in the Southern Hemisphere tropical region on the other hand is entirely due to a depletion in preformed DIC. This region also experiences a strong warming thus reducing the solubility of CO₂ within the surface waters and limiting the amount of DIC that can be held by the water in equilibrium with the atmosphere and at constant alkalinity. To verify that the reduction in solubility is driving the subsequent decrease in DIC, we show the DIC content versus heat content for the tropical region in Figure 3.10 (a). The strong negative relationship supports the hypothesis that the variability in preformed DIC in this region is driven by changes in solubility. Figure 3.10 (a) additionally shows the theoretical change in carbon content given a change in heat content due to solubility alone (constant pCO₂ and alkalinity – black line) with a slope of

3.4. MECHANISMS DRIVING VARIABILITY

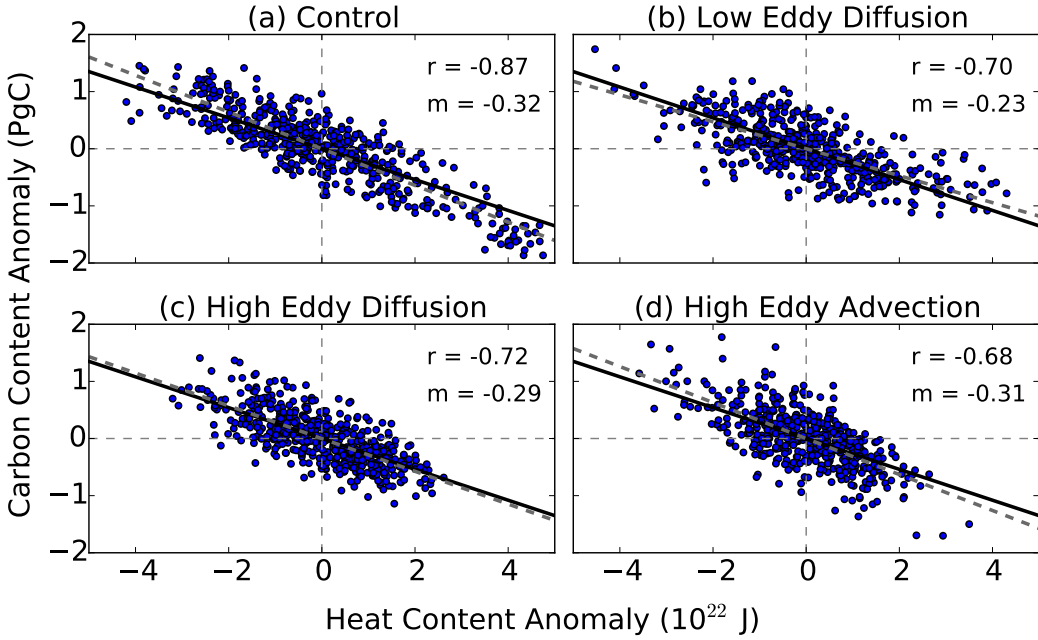


FIGURE 3.10: Scatter of heat content anomaly vs preformed DIC integrated over the tropical region for each simulation. Dashed grey linear line represents the linear fit of the carbon vs heat data with slope, m , and pearson correlation coefficient r . Solid black linear line represents the projected change in carbon content given a change in heat content with constant alkalinity and pCO_2 in equilibrium with the preindustrial atmosphere (scaled from *Gruber et al.* [1996]).

$-0.27 \text{ PgC}/10^{22}\text{J}$. This relationship is calculated using the relationship derived in *Gruber et al.* [1996] and scaled to relate carbon content with heat content. There is good agreement between this theoretical model and the linear regression of carbon content versus heat content for this region, represented by the dashed grey line (linear slope values, m , also shown on Figure 3.10), further supporting the hypothesis that carbon variability is consistent with variability in solubility.

The above solubility mechanism appears to hold in all simulations (Figure 3.10 (b) – (d)). All simulations have the same negative relationship between preformed carbon content and heat content integrated over the tropical region ($20^\circ\text{S} – 20^\circ\text{N}$) with good agreement with the scaled solubility line (black line). This result suggests that the variability in DIC in this region is driven by variability in the temperature-driven solubility, regardless of the high-latitude convective variability.

Finally we examine the southern mid-latitude subsurface increase in DIC seen in Fig-

3.4. MECHANISMS DRIVING VARIABILITY

ure 3.8 (b). Looking at the components of DIC, it is apparent that this increase is entirely due to remineralized DIC. To understand why this increase of remineralized DIC occurs, we correlate the remineralized DIC anomaly with ideal age in the southern mid-latitude subsurface region (averaged between 40°–50°S and 200–1000 m, Figure 3.11). The ideal age is a tracer in the model simulation which quantifies the mean time since the water last had contact with the surface. The tracer is set to zero in the mixed layer and ages at a rate of 1 yr yr^{-1} after it leaves the mixed layer. In all simulations, the remineralized DIC anomaly in this region is strongly correlated with ideal age with Pearson correlation coefficients exceeding 0.8 (Figure 3.11). Calculating the linear regression coefficient (m) between the remineralized DIC and ideal age yields a rate of accumulation of remineralized DIC of approximately $0.25 \mu\text{mol kg}^{-1} \text{ yr}^{-1}$ for all simulations (Figure 3.11). Comparing this rate of accumulation of remineralized DIC to the modeled local remineralization rate ($jPO_4 \times 108 = 1.6 \mu\text{mol kg}^{-1} \text{ yr}^{-1}$) we find that the rate of accumulation of remineralized DIC in this region is significantly less than the remineralization rate. The DIC found at a given point has accumulated along many trajectories, some largely passing through surface waters where the local remineralization rate is large, and some passing through deep waters where the local remineralization rate is small. The low slope of the relationship between $\text{DIC}_{\text{remin}}$ and age suggests that it is changes in the fraction of waters taking deeper trajectories that is most important in explaining the changes in Figure 3.11.

Because only changes in transport cause the ideal age to change, the strong correlation between the remineralized DIC and ideal age suggest the accumulation of $\text{DIC}_{\text{remin}}$ is due to a slow down of exchange between the surface and subsurface waters. This conclusion is only valid if the rate of local remineralization is constant, or does not impact the time tendency of DIC in this region. Correlation analysis between the modeled remineralization rate and DIC tendency suggest no significant (or very small) correlation between the two variables (see supplemental material Figure 5) indicating the variability in subsurface $\text{DIC}_{\text{remin}}$ is indeed due to variability in transport.

3.4. MECHANISMS DRIVING VARIABILITY

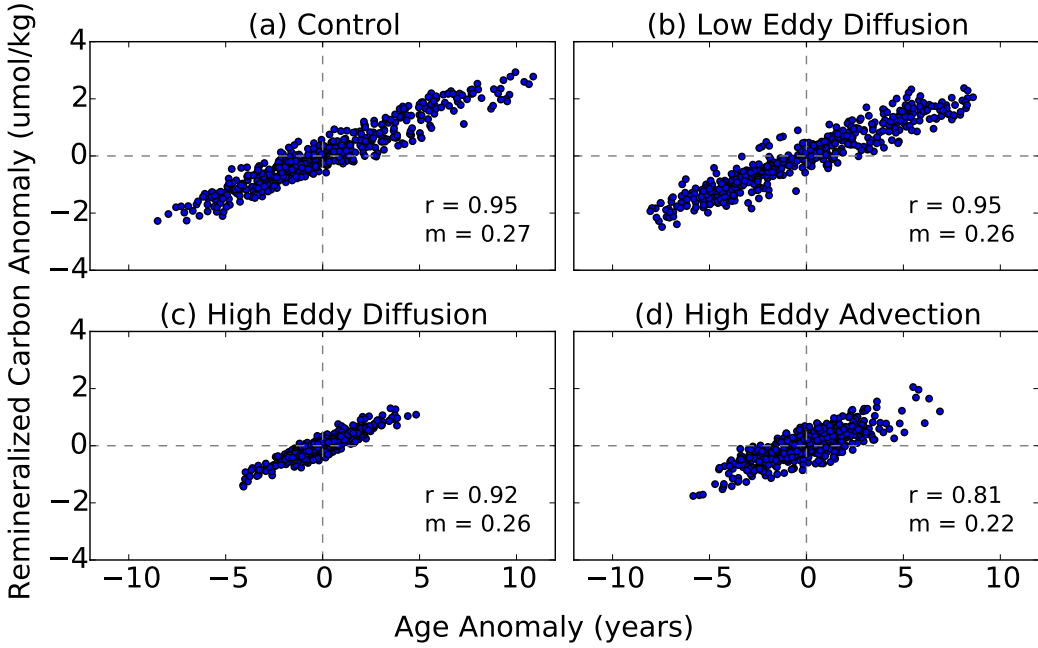


FIGURE 3.11: Ideal age versus remineralized DIC for all simulations. Quantities are averaged over latitudes 40° – 50° S and 200–1000 m. Linear regression coefficients, m , and pearson correlation coefficients, r , are included for reference.

To verify that the same spatial relationship of DIC and its components is consistent in all simulations, we show the covariance of globally integrated DIC against zonally (and vertically) integrated DIC, DIC_{pre} , and $\text{DIC}_{\text{remin}}$ in Figure 3.12. The general pattern of covariance between the global DIC and remineralized DIC shows a strong positive value in the Southern Ocean followed by a decreasing to negative covariance in the southern mid-latitudes and then increasing again to above zero in the tropics. This pattern is apparent in all simulations, but with different magnitudes due to the different convective variability. When comparing with Figure 3.8 it is important to note that these covariance calculations use the DIC integrated over the entire water column, whereas Figure 3.8 only shows the surface layer (top 1500 dbars). Due to deep spreading of decreased $\text{DIC}_{\text{remin}}$ values from the Southern Ocean convection into the abyssal mid-latitudes (supplemental Figure S6), the depth-integrated global DIC and remineralized DIC covariance does not become negative until approximately 45° S.

The opposite pattern holds for the covariance between global DIC and preformed

3.5. CONCLUSIONS

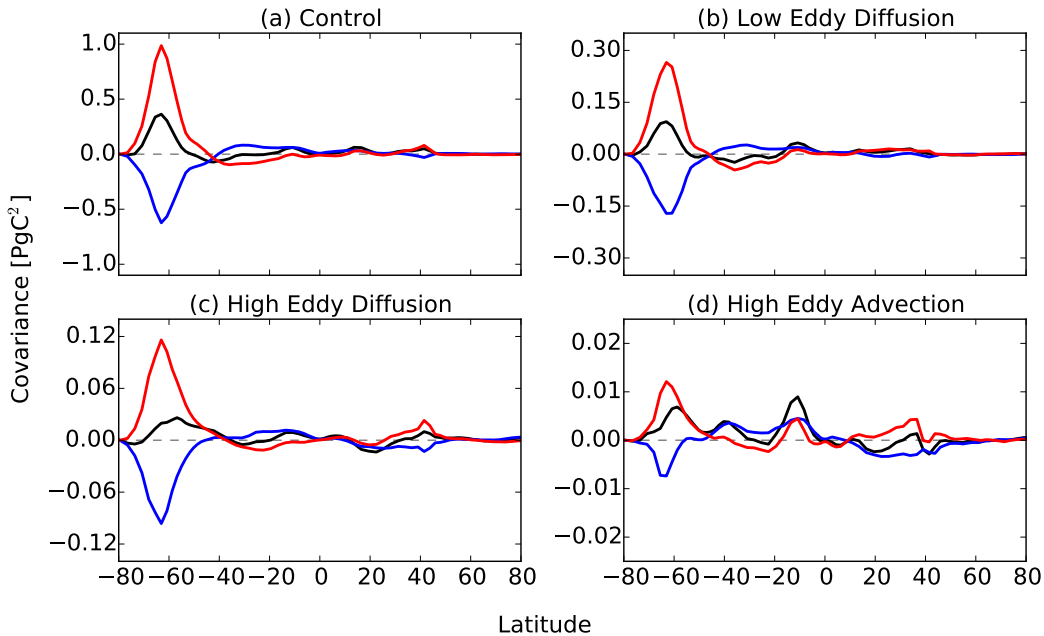


FIGURE 3.12: Covariance between globally integrated DIC content and DIC (black), preformed DIC (blue) and remineralized DIC (red) for each simulation as a function of latitude. Note different y-axis scales.

DIC: a negative covariance in the Southern Ocean, followed by an increase in covariance in the southern mid-latitudes and a decrease below zero north of the equator. Because of the lack of deep convection in the *high mixing simulations*, the Southern Ocean covariance is significantly smaller than the other simulations (note different y-axis scales in Figure 3.12), but the qualitative relationship remains the same. The consistency in the general shape of these relationships suggests that the same mechanisms are controlling the regional variability in all simulations.

3.5 Conclusions

Using a coupled climate model, we have quantified the global and regional natural variability in oceanic heat and carbon content. We have found that in this model, the highly convective Southern Ocean drives strong global variability in heat and carbon content. Additionally, these two quantities are strongly anti-correlated. Using simulations with different parameter settings for mesoscale mixing, we show that these results are robust

3.5. CONCLUSIONS

across simulations with different WS convective variability, but the anti-correlation relationship is strongest with the two simulations which oscillate between convecting and non-convecting states.

As illustrated in Figure 3.13, the global anti-correlation between heat and carbon content is due to differences in the sign and magnitude of the regional variability. The arrows in the schematic indicate the magnitude of variability and the sign during a convective period. As indicated, the global heat and carbon content are anti-correlated.

In the Southern Ocean, heat and carbon content are both depleted during convection, but the southern mid-latitude and tropical regions each have heat content variability that balance the Southern Ocean variability. The resulting global heat content variability therefore has the same sign and magnitude as the variability in the southern mid-latitudes and tropics. Carbon content variability on the other hand exhibits a cancelation between the southern mid-latitudes and tropics. Therefore, the resulting variability in global carbon content closely follows the variability in the Southern Ocean.

The sub-surface variability structure is also depicted in Figure 3.13 and highlights the differences between heat and carbon. During convection, both quantities decrease in the subsurface Southern Ocean. Additionally, both heat and carbon show increases in the southern mid-latitudes, but the temperature increases are contained in the surface, while DIC increases at depth. This increase in subsurface DIC is likely a result of decreased ventilation. Finally, the southern mid-latitudes and tropics show an increase in surface temperature and a decrease in surface DIC. The variability in DIC here is due to solubility decreases as a result of the temperature increase.

Comparing the magnitude of the modeled natural variability to the size of recent observed trends can provide information on how detectable anthropogenic trends are [Thomas *et al.*, 2015]. For the control simulations, the magnitude of global carbon variability is about ± 3 PgC. This accounts for only approximately 3% of the estimated an-

3.5. CONCLUSIONS

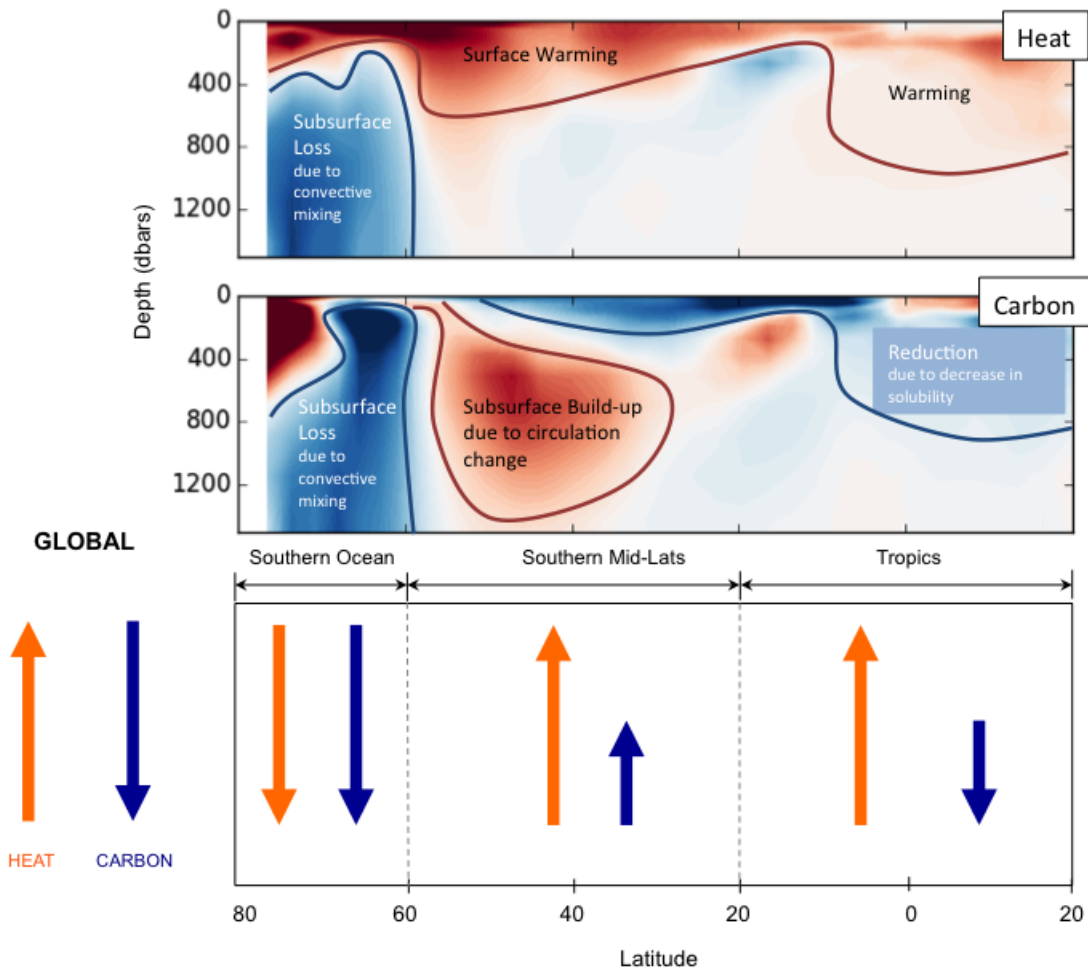


FIGURE 3.13: Schematic summarizing regional variability in oceanic heat and carbon during a convective year. Arrows designate the sense of global and regional inventory change during a convective year, positive indicating an increase in oceanic content.

3.5. CONCLUSIONS

thropogenic uptake of carbon over the past few decades [Khatiwala *et al.*, 2012; Sabine *et al.*, 2004; Waugh *et al.*, 2006]. The variability in global heat content on the other hand is about $\pm 3 \times 10^{22}$ J. This is a much larger percentage (20%) of the estimated uptake of anthropogenic heat in recent decades [Levitus *et al.*, 2009]. These results suggest that changes in carbon content due to anthropogenic activity are unlikely to be obscured by long-timescale variability, but changes in heat content could be obscured. This large natural variability in global heat content could explain why there is less CMIP5 model agreement in oceanic heat uptake than there is for carbon uptake [Frölicher *et al.*, 2009].

If we assume these results hold for the real ocean, we would expect that during the current non-convective period we would experience a subsurface warming in the Southern Ocean and a slowdown of the intermediate water ventilation. Both these processes have been documented in observational studies [Purkey and Johnson, 2012; Waugh *et al.*, 2013], but it is important to note that these changes could also be due to anthropogenic influences such as greenhouse gas warming and ozone depletion in addition to variability in WS convection. The frequency of modeled WS convection is hard to compare to real-life WS convection because of the lack of an observational record in the Southern Ocean. Additionally, *de Lavergne et al.* [2014] have shown that models that have frequent convection in preindustrial control simulations have a significant reduction in convection under global warming scenarios. This suggests that we may not observe another strong WS convective event, and makes it extremely difficult to determine what frequency of WS convection is ‘correct’.

The results of this study suggest that the atmosphere could exhibit significant changes in temperature and CO₂ concentration in response to Southern Ocean convective variability. A previous study by Cabre *et al.* [2017] using our control version of the ESM2Mc model shows an increase in SH and global atmospheric temperatures. This is because the additional flux of heat into the ocean is more than balanced (and indeed is driven) by a decrease in clouds and ice, resulting in an additional 0.15 PW of additional shortwave

3.5. CONCLUSIONS

heating of the Southern Hemisphere when convection is at its peak. An interesting extension of this study would be to examine whether relatively small preindustrial changes in atmospheric carbon dioxide could be associated with changes in SH temperatures, as well as a more comprehensive examination of this process in Earth System Models with variable atmospheric carbon dioxide.

A caveat with this study is that only a single model has been used. More analysis should be conducted with additional model simulations to examine if this relationship and the relative magnitudes of variability between heat and carbon are consistent. Similar analysis with additional models could help to understand the intermodel spread of oceanic carbon content, and the larger intermodel spread in oceanic heat content [*Frölicher et al., 2014b*], and also provide a better context in which to analyze recent observational trends. Additionally, the model used in this analysis has a relatively coarse resolution and parameterizations for mesoscale eddies. *Dufour et al. [2017]* assessed the impact that model resolution has on WS convection and concluded that horizontal model resolution has an important impact on vertical stratification and the subsurface heat reservoir build-up. However, the impact of resolution is not straightforward - a 1/4 degree ocean behaved more like our high eddy diffusion model with relatively constant convection while a 1/10 degree ocean model showed more stratification and behaved more like our control model. *Griffies et al. [2015]* have additionally examined the impact eddies have on Southern Ocean heat uptake and transport in eddy-permitting models and have concluded that uncertain model parameterizations tend to lead to model drift and less accurate lateral and vertical heat distribution. These impacts need to be kept in mind when discussing model simulations with parameterized eddies.

CHAPTER 4

Relationship between age and oxygen

4.1 Abstract

The relationship between age and oxygen is one that is often assumed in oceanography to be relatively simple. Because oxygen utilization rates are difficult to directly measure in the ocean, it is commonly assumed that the apparent oxygen utilization divided by the water age is a good representation of respiration. Likewise, because of limited transient tracer observations and difficulties constraining water age, it has been suggested that oxygen could be a useful proxy for age. In this paper, we explore the relationship between age and oxygen along observational Line W, a repeat hydrography cruise track which transects the Gulf Stream, extending from Cape Cod to Bermuda and in an Earth System Model simulation to determine if these assumptions can safely be made. We find that in both the observations and model, the assumed negative linear relationship between age and oxygen is not found both within and directly below the ventilated thermocline at the end of Line W. This result is consistent with our model simulation, which also shows that the relationship between age and oxygen is more complicated than often assumed. While observations along Line W shows a decoupling of the biologically-driven age-oxygen re-

lationship, our model analysis indicates that this phenomenon is relatively localized to Line W due to the combination of relatively weak horizontal gradients in age and oxygen resulting reduced along-isopycnal variability and vertical heave acting on a depth offset between age and oxygen extrema.

4.2 Introduction

When examining the relationship between age and oxygen it is generally assumed that the two follow a negative relationship. Oxygen concentration is set at the surface and generally decreases in the ocean interior due to biological consumption. Age on the other hand, is set to zero at the surface and increases in the ocean interior, characterizing the time spent since last in contact with the surface. This relationship between age and oxygen is exploited in the oceanography in two ways. The first is that allows for the indirect measurement of the oxygen utilization rate to diagnose changes in ocean productivity, and the second is that it allows for the possibility to use oxygen as a proxy for age when examining changes in ocean circulation. The primary sink of oxygen is the utilization by biology. For this reason, the oxygen utilization rate (OUR) is a powerful tool for understanding ocean biology and biogeochemistry. In the ocean interior, the OUR is generally very small and therefore very difficult to directly measure. A commonly used solution to this is to estimate the OUR as the derivative of the change in AOU over the change in age:

$$\text{OUR} = \frac{d\text{AOU}}{d\Gamma} = \frac{d([O_{2\text{sat}}] - [O_2])}{d\Gamma} \quad (4.1)$$

This definition of OUR is fairly ubiquitous in the ocean biogeochemistry community. It is referenced in multiple textbooks (Sarmiento and Gruber, 2006; Emerson and Hedges, 2008), and has been used extensively in the literature to draw conclusions on organic matter transport from the surface ocean to the deep (Jenkins, 1982), and quantify biological productivity in the ocean (Burd et al, 2010). However, as discussed in Koeve

4.2. INTRODUCTION

et al.(2016), this method for determining OUR assumes that the advective and diffusive transports impact the age and oxygen in the same way. This will only be strictly true if the two tracer fields have the same distribution of internal sinks, something which is general is not the case. The authors found that when averaged over three coupled physical and biogeochemical ocean models, the OUR determined by this method underestimated the actual modeled OUR by a factor of 3. This result suggests that the relationship between age and oxygen is not as straightforward as often assumed.

Another way that oxygen and age have been combined in the field is through the suggestion that oxygen could be used as a proxy for age for quantifying changes in ocean circulation. While transient tracers are a useful tool for understanding ocean circulation, there are some well-documented complications in estimating age from such tracers (REF: Haine and Hall?). Additionally, transient tracer measurements are made much less frequently than oxygen measurements, making it impossible to directly estimate ocean age from the historical record. To resolve these problems, the possibility of exploiting the age-oxygen relationship and using oxygen as a proxy for age has been suggested in the physical oceanography community. Changes in oxygen concentration could be used to diagnose changes in ocean circulation when age measurements are unavailable (example: Deutsch, Emerson and Thompson, GRL, 2005; Kwon, Deutsch et al., J. Climate, 2016). However, in order for this methodology to be successful, the negative correlation relationship between age and oxygen would need to be robust over time and space. Because age and oxygen concentration are subject to diffusive mixing and advective transport processes, the both of these hypothesized relationships only hold when advection is the dominant process, or when remineralization rates are spatially and temporally uniform. In this paper, we evaluate the relationship between age and oxygen to shed light on where it may be valid to use oxygen as a proxy for age and to consider the use of defining OUR as AOU divided by mean age. Because it crosses the western boundary current in the North Atlantic Ocean, and has measured both transient tracer and oxygen concentrations, Line W

4.3. METHODS

provides a unique opportunity to investigate the assumed negative relationship between age and oxygen and examine the robustness of the two mentioned applications of this age-oxygen relationship. Because of the limited spatial and temporal resolution of the Line W observational data, we supplement the observational data analysis with analysis of an earth system model, GFDL ESM2Mc.

In the next section we introduce the Line W observational data set, describe how transient tracer ages were derived, and discuss the earth system model specifications. In Section 3 we explore the age-oxygen relationship in the observations and model, and discuss mechanisms driving the resulting relationship. Finally, in Section 4 we share our conclusions.

4.3 Methods

4.3.1 *Line W Observational Data*

4.3.1.1 *Data Collection*

The observational data set used in this analysis comes from the Woods Hole Oceanographic Institute's (WHOI) Line W ship-based repeat hydrography study. Observations include full-depth temperature and salinity profiles, horizontal velocity profiles from lowered ADCPs (LADCPs), and bottle-sampled transient tracer and oxygen concentrations. Data was collected once or twice-per-year (one cruise in the spring and one in the fall) over the 2003-2012 period. The Line W cruise line extends from just south of the coast of Cape Cod (40.29 N, 70.21 W) and extends to Bermuda (32.16 N, 65.23 W - Figure 1 (a)). The water property and velocity measurements were taken at 26 fixed sites along Line W. The stations are more densely situated across the continental shelf to resolve the Deep Western Boundary Current. The station spacing becomes greater and temporal sampling frequency is lower along the end of the Line W tract, near Bermuda. Temperature and salinity data was collected using a conductivity-temperature-depth (CTD) instrument mounted on a

4.3. METHODS

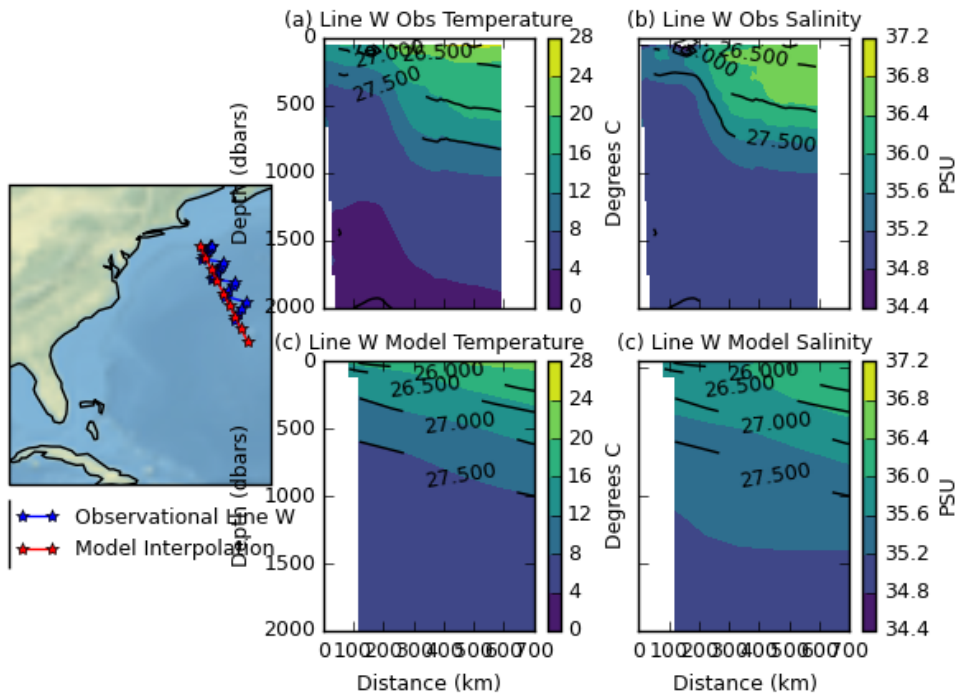


FIGURE 4.1: Observational Line W and model interpolation. (a) and (b) climatologies of observational temperature and salinity. (c) and (d) Line W interpolated model temperature and salinity.

rosette frame. Salinity (i.e. conductivity) measurements were then validated with bottle measurements of salinity (Millard and Yang, 1993). Bottle measurements were sampled using 10-L Niskin bottles mounted on a rosette. Generally, 23 bottle samples at various depths were taken at each location along the cruise line. Water samples were analyzed on board for salts, dissolved oxygen, and transient tracer concentrations. The transient tracers sampled include multiple chlorofluorocarbon compounds: CCl₃F (CFC-11), CCl₂F₂ (CFC-12), and CCl₂FCClF₂ (CFC-13). For a full description of the Line W data set please reference Andres et al, 2017. The data is available on the WHOI Line W website (<http://www.whoi.edu/science/PO/linew>).

4.3.1.2 Data Processing

For purposes of visualization and comparison with the Earth System Model, the data has been interpolated to a grid with a vertical resolution of 100 dbars and horizontal resolu-

4.3. METHODS

tion of 10 km. Cross-sections of oxygen concentration and mean age (described below) for two years are shown in Figure 2. Oxygen is generally high at the surface and decreases with depth, reaching a minimum between depths 250 dbars and 750 dbars. Age on the other hand is at a minimum at the surface and increases with depth. (NOTE SMALLER-SCALE FEATURES SEEN IN BOTH PLOTS). Figure 2 additionally shows the time-series of two locations along Line W (as indicated by the black boxes). The first time-series (Figure 2 (e)) suggests that there is a positive correlation between age and oxygen. The second time-series (Figure 2 (f)) on the other-hand shows the anticipated negative relationship between age and oxygen. Because temperature and salinity impact oxygen saturation, we additionally compute the Apparent Oxygen Utilization for the observational data:

$$AOU = O_{2sat} - O_2 \quad (4.2)$$

where O_{2sat} is the equilibrium saturation concentration of oxygen, calculated as a function of temperature and salinity, and O_2 is the observed oxygen concentration. The AOU is a measure of how under-saturated the oxygen sample is. Using the AOU instead of oxygen concentration allows us to ignore the impacts of temperature on the oxygen measurement.

4.3.1.3 Mean Age Calculation

A critical component to understanding ocean circulation and quantifying biological respiration is estimating the age of the water - or how long since the water was last in contact with the surface. Doing this with observations is not easy, but transient tracers make it possible. Because of the atmospheric time history of Chlorofluorocarbons (CFCs), and the fact that CFCs have no sources and sinks in the ocean, CFCs are often used to quantify the age of ocean water. The simplest way of doing this is to assume that CFCs are in equilibrium with the atmosphere when they leave the ocean surface and are then transported

4.3. METHODS

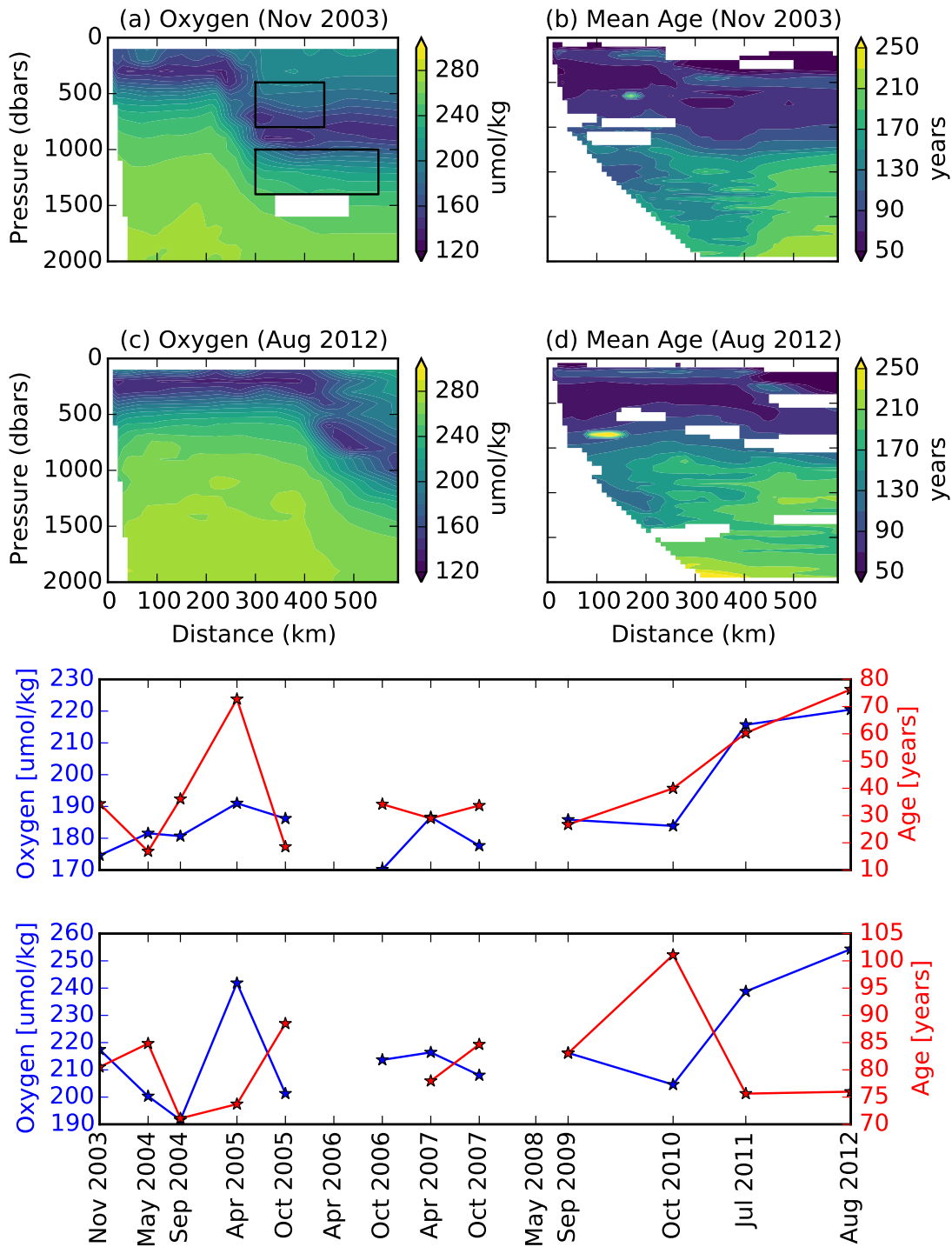


FIGURE 4.2: Observational age and oxygen for two years.

4.3. METHODS

advectively to the observation site. One can then deduce the date at which the water was subducted by matching the partial pressure of CFCs in the water to the date at which they had that concentration in the atmosphere. This assumes that the transport to a given point can be characterized by a single timescale- the advective time. In reality, estimating the age is complicated by mixing in the ocean. Because all flow is a combination of advective and diffusive flow, there is no one timescale that characterizes the time that a parcel of water has taken to reach an interior location from the surface. Because of this advective and diffusive flow, we characterize the timescales of a given point in the ocean interior with a distribution of transit times (or transit time distribution). The basis for this transit time distribution (TTD) approach for estimating ocean age is that for steady transport, the interior concentration of a transient tracer, $c(r, t)$, is given by (Haine and Hall, 2002):

$$c(r, t) = \int_0^{\infty} c(t-t') G(r, t') dt' \quad (4.3)$$

where $G(r, t)$ is a function describing the TTD at location r and time t . Measurements of CFC-12 were used to estimate the TTD assuming that (1) the TTD follows an Inverse Gaussian distribution and (2) the ratio of the mean width to mean age ($\Delta\Gamma$) of the Inverse Gaussian is approximately equal to 1 (Waugh et al, 2003; Waugh et al, 2004; Waugh et al, 2006). Making the assumptions in order to estimate $G(r, t)$ using the Line W CFC-12 data and using the atmospheric history of CFC-12 allows us to estimate the mean age of the water sample.

4.3.2 Model Data

In addition to the observational data, we use an Earth system model (GFDL ESM2Mc) to quantify the relationship between oxygen and age. GFDL ESM2Mc (Galbraith et al, 2011) is a coarse resolution configuration of the GFDL ESM2M (Dunne et al., 2012). The model has an atmospheric resolution of 3.875 x 3 with 24 vertical levels. The ocean model is non-

4.4. RESULTS

Boussinesq, using pressure as the vertical coordinate, and has a resolution of 3 x 1.5 and 28 vertical levels. The oceanic model also has a coupled biogeochemical module referred to as the Biogeochemistry with Light Iron Nutrients and Gases (BLING) model (Galbraith et al., 2010). Although this module uses a highly parameterized biological cycle, it predicts patterns of carbon and oxygen change in response to global warming that are very similar to a more complex biogeochemistry simulation in ESM2M (Galbraith et al., 2015). The model also computes an ideal age (Thiele and Sarmiento, 1990), setting this tracer to zero in the surface box and allowing it to increase at 1 yr/yr in the ocean interior. For a full description of the model simulation, please reference Section XX (from chapter 3).

The model is interpolated to 1x1 grid in the North Atlantic and then interpolated to a line extending from position (40 N, 69 W) to (22 N, 60 W) to match observational Line W (Figure 1 (a)). The model shows a similar temperature and salinity profile on Line W compared with the observations (Figure 1 (b) - (e)). The model simulation is used as a supplement to the observational data analysis and to investigate potential mechanisms affecting the age-oxygen relationship.

4.4 Results

4.4.1 Age and Oxygen Relationship

The climatologies of the calculated mean tracer age and oxygen concentration from the Line W observations are shown in Figure 3 (a) and (b). Observing the two plots, in general there appears to be a negative relationship between the age and oxygen. There is relatively high oxygen concentration and zero age at the surface, consistent with the surface waters being in contact with the atmosphere, resulting in near-equilibrium in oxygen and CFC concentrations. Age then generally increases with depth, reaching a local maximum at just below the average depth of the 27.5 neutral density surface. Oxygen on the other hand generally decreases with depth, reaching a local-minimum along the average depth

4.4. RESULTS

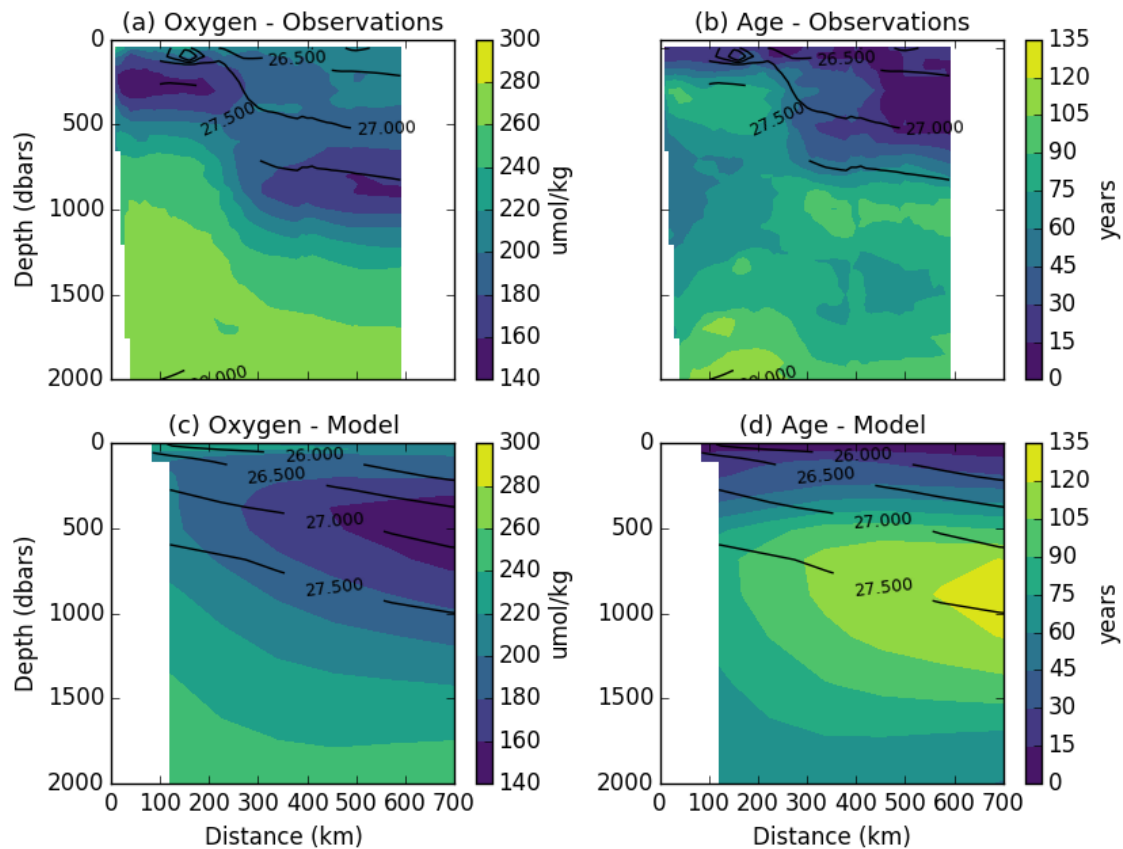


FIGURE 4.3: (a) Oxygen climatology and (b) age climatology from observations along Line W. Contour lines show average neutral density.

4.4. RESULTS

of the 27.5 neutral density surface. The spatial patterns of age and oxygen generally point towards a negative relationship between the two qualities, particularly at intermediate depths. Oxygen shows a core of minimum values with two intense patches, where the concentrations drop below 160 M, on either side of the Gulf Stream more or less aligned with the 27.5 neutral density surface. Age also shows two such patches of high values on either side of the Gulf Stream at similar depths. However, there are interesting differences in the detailed structure. First, the age maximum found just below the ventilated thermocline at distances 300-500 km occurs at a depth of 1000 dbars. This is lower in the water column than the oxygen minimum, which occurs at an approximate depth of 800 dbars. Additionally, there is significantly more spatial variability in the age in the deeper regions across all distances than is seen in the oxygen climatology. These differences between the spatial patterns suggest the relationship between age and oxygen is likely more complicated than has been suggested in previous work. As discussed in the introduction, because of the limited temporal and spatial resolution of the observational data, we also examine the age-oxygen relationship in an Earth System Model. The vertical structure of the modeled oxygen and age climatologies (Figure 3 (c) and (d)) are similar to the observed climatologies, though somewhat offset in density space. The modeled oxygen concentration exhibits a local minimum close to the 27.0 average neutral density surfaces, while the age reaches a local maximum on the 27.5 average neutral density surface. While the vertical structure of age and oxygen in the model are similar to the observations, there is a more obvious offset between the depths of the local oxygen minimum and local age maximum in the model. As with the observational data, this suggests a possible breakdown of the suggested negative relationship between age and oxygen in this region. Note also that our relatively coarse model does not allow for separation of two cores of low oxygen water by the Gulf Stream, arguably, only the offshore core seen in the observations is simulated with some measure of fidelity.

To better quantify the temporal relationship between mean age and oxygen, the Pear-

4.4. RESULTS

son correlation coefficient between age and oxygen is calculated along Line W (Figure 4 (a)). Although this figure shows the anticipated negative correlation between age and oxygen, in much of the plot the correlations are relatively low. Moreover, two regions of positive correlation are apparent between 200 and 400 km offshore. One positive correlation region is at approximate depths 500-750 dbars (between neutral density surfaces 27.0 and 27.5), and the second is slightly deeper at depths 1250 - 2000 dbars. Given the anticipated anti-correlation between age and oxygen, especially in the ventilated thermocline, both the low correlations through much of the sections and the regions of positive correlation are surprising.

One possible reason for the lack of a tight relationship between oxygen and age is that oxygen concentration depends on solubility and thus on temperature and salinity. In order to correct for this effect, we also examine the relationship between the age and apparent oxygen utilization (AOU). The AOU is a measure of how under-saturated the oxygen concentration is. This under-saturation is usually due to the biological consumption of oxygen but may also see an effect from incomplete equilibration of sinking source waters, particularly in convective regions. Analyzing the relationship between AOU and age gives us similar information to the age-oxygen relationship, however, because we are subtracting the oxygen concentration from the oxygen saturation, the AOU-age relationship will be the opposite sign (mainly positive) and the AOU-age relationship removes the impacts of temperature (and salinity) on oxygen saturation.

The Pearson correlation coefficient between age and AOU (Figure 4 (b)) shows a positive relationship between the two quantities. Similar to the pattern seen in the age-oxygen correlation coefficients (Figure 4 (a)), there are two regions with anomalous correlation. One upper region of near-zero correlation, corresponds with the upper region of positive correlation seen in Figure 4 (a). This suggests that this positive correlation between age and oxygen in this region largely results from temperature effects. Younger waters in this region are colder and thus hold more oxygen-countering any impacts from less rem-

4.4. RESULTS

ineralization. Note however, that even with temperature effects removed the AOU-age correlation remains low. Moreover, the region with anomalous O₂-age correlation in the deeper waters also shows an anomalous AOU-age correlation (negative). The fact that these patterns exist in the age-AOU correlation pattern in addition to the age-O₂ correlation pattern suggest that we need to find a mechanism other than solubility changes for explaining such variability.

We also show the Pearson correlation coefficient for the model simulation (Figure 4 (c) and (d)). Although the model also shows the expected negative correlation between age and oxygen over much of the domain, the correlation is far from uniform with one core of strong positive correlation in denser waters around 1000 dbars and a second layer of negative correlation at around 300 dbars. As in the observations, there is a region of positive correlation (with correlation coefficient of approximately 0.4) between the negative correlation layers, starting at distance 400 km and extending to the end of Line W. This region of positive correlation is similar to the upper region of positive correlation seen in the observational record. Interestingly, in the model simulation, there is no deeper region of positive correlation as seen in the observational correlation, although there is a decline in the correlations as one approaches the coast below 1500 dbars.

The modeled age-AOU temporal correlation shows a very consistent pattern with the modeled age-oxygen correlation. The area of anomalous correlation (now negative) around depth 500 dbars is greatly reduced in Figure 4 (d), suggesting that a fraction of the positive correlation seen in the age-oxygen correlation is due to solubility- a signal similar to that seen in the observations. However, as in the observations this region still has a reduced positive correlation, suggesting some additional mechanism is impacting the age-AOU relationship.

4.4. RESULTS

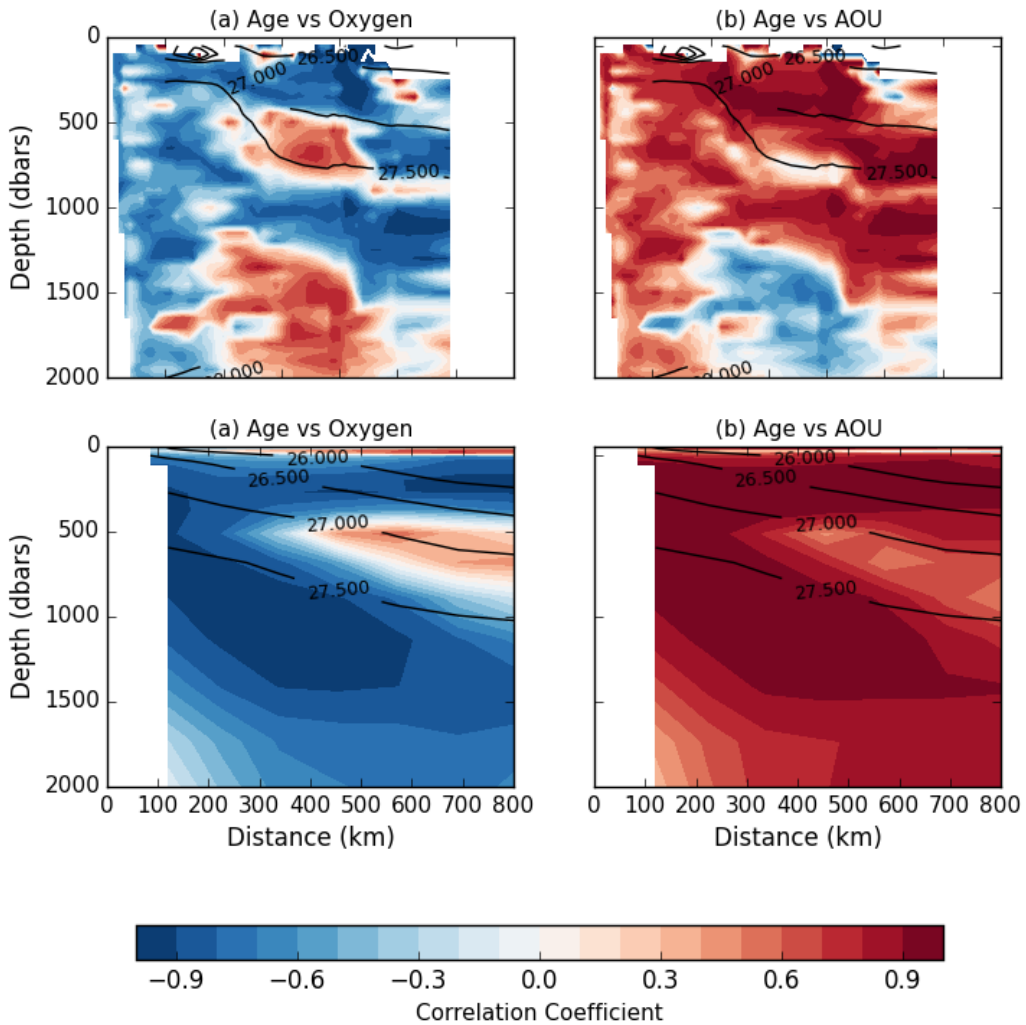


FIGURE 4.4: Pearson correlation coefficients for age versus (left) oxygen and (right) AOU for Line W observations. Contour lines indicate average neutral density climatology.

4.4. RESULTS

4.4.2 Age and Oxygen/AOU Scatterplots

To better visualize and analyze the relationship between the mean age and oxygen along observational Line W, we show the scatter plot of age versus oxygen in Figure 5 (a). The scatter points are colored with each location's temporal correlation coefficient (same as in Figure 4 (a)). The 'S-shape' of the age-oxygen scatterplot relationship roughly follows the depth of the water column, with the surface waters at the left end of the 'S-shape' and the deep waters at the right end. The positive correlation regions indicated from Figure 4 (a) also appear in this relationship.

The scatter plot relationship between age and AOU is also shown (Figure 5 (b)). Similar to the age-oxygen scatter plot, the age-AOU scatter plot also roughly follows depth, with the surface waters at the left-hand side of the scatter plot, transitioning to the deeper waters at the right hand-side. The upper region of reduced/zero correlation discussed with Figure 4 (b) is seen on this diagram at an age of 50 years, just before the maximum in AOU. Additionally, the deeper region of negative correlation discussed in Figure 4 (b) is seen on this diagram on the almost-flat tail end of the scatterplot. Visualizing the age-AOU relationship in this way is a powerful tool because it allows us to gain initial insight to the mechanisms governing the AOU variability. The dashed lines represent expected linear relationships between age and AOU with the slope of the linear relationship being directly proportional to the rate of remineralization. At the surface, where sinking particulate matter has higher concentrations and is more easily decomposed, we have increased rates of remineralization, and therefore we would expect the age-AOU relationship to follow one of the linear relationships with a higher slope. As we move deeper in the water column, the slopes should decrease to reflect the slower rates of remineralization in the deep ocean.

If the variability in AOU were driven exclusively by changes in the rate of ventilation (but not the pathways of ventilation or the rate of remineralization), we would expect

4.4. RESULTS

the age-AOU relationship to fall along one of the dashed lines. The upper region does follow this linear relationship (with a slope of 1.7 M/yr). When the age-AOU relationship does not follow these linear lines however, it indicates that other processes are influencing the spatial (and thus potentially the temporal) variability in AOU. The right-hand tail of this relationship, where the correlation is negative, does not follow the anticipated linear relationship, and therefore we can infer that some additional process is influencing the AOU-age relationship. This region is also one where the correlation between AOU and age is (unexpectedly) negative.

The shape of the modeled relationship between age and oxygen is similar to the shape of the observed age-oxygen relationship (Figure 5 (a)), suggesting that the model captures the mean relationships to a surprising extent (given the coarseness of its resolution and the simplicity of its biological model). However, there are clear differences between the modelled and observed variability. In the model, the area of positive correlation between the age and oxygen occurs in the region of the oxygen minimum, which is a region where the age is still increasing with depth. Since the shape of the relationship roughly follows depth, movement along this curve would correspond to vertical movement in the water column. In this region, if we move lower in the water column, age increases and oxygen also increases, therefore resulting in a positive correlation. This suggests that vertical movement in the water column could be causing the positive correlation. In the observations, however, the upper region of positive correlation is found above the oxygen minimum and the lower region is found around a weak age minimum. The corresponding point on the modelled age-oxygen plot shows some near-zero correlations, but no positive values.

The modeled age-AOU scatter plot (Figure 5 (d)) has similarities to the observed age-AOU relationship (Figure (b)), but has a much more pronounced mid-depth age minimum. As in Figure 5 (b), the dashed grey lines represent the linear relationship between the age and AOU. In the upper region of the domain, the age and AOU follow this linear relation-

4.4. RESULTS

ship quite closely (with a slope of 1.7 M/yr -similar to the observations). Slightly deeper in the water column, the age and AOU also closely follow a linear line, with a slightly smaller slope (slope of 0.8). In the deeper waters however, the age-AOU relationships break away from the linear model, suggesting additional processes impacting the AOU variability.

Some part of the mean relationship is driven by the well-known decrease in the remineralization of organic material with depth (see for example Armstrong et al., Deep Sea Res., 2002) as unprotected organic materials are preferentially consumed near the surface. This would move points between a steeply-sloped linear relationship near the surface to lying along a line with a flatter slope at depth. An additional factor is that the pathways of ventilation change with depth, with waters near the deep age minima more affected by the southward flow of North Atlantic Deep Water. These different factors have the potential to affect the variability as well. In particular, changing pathways of ventilation would be expected to change the mix of water masses seen at a given point. Assuming the water masses involved in this mixing are reflected in the AOU-age structure, such changes might be expected to produce relationships parallel to the age-AOU curve- which in many locations would imply anti-correlation (where the mean curve slopes down to the right) or near-zero correlation (where the mean curve is oriented either horizontally or vertically). We note that when the age-AOU curve lies along one of these dashed lines, it is impossible to distinguish changes in ventilation rate from changes in water mass type without bringing in more information. The region of reduced positive correlation seen in the depth profile of the age-AOU Pearson correlation coefficient (Figure 4 (d)) is seen in the age-AOU scatterplot (Figure 4(d)) at the apex of the scatter plot, where the AOU goes from increasing with age to decreasing with age. This region occurs between the two regions of strong linear relationship between age and AOU as discussed above. This result suggests that it is a change in the fraction of water associated with two water masses that is contributing to the reduced positive correlation in age versus AOU (or positive in the age-oxygen correlation).

4.4. RESULTS

This analysis provides some initial insight to why the age-oxygen relationship displays an area of positive correlation. The age-AOU scatter plot suggests that mixing between water masses may be contributing to the anomalous correlation in the age-oxygen and age-AOU relationships. In the next section, we will investigate the mechanisms driving the modeled variability in age and oxygen further, examining whether the results can be simply explained in terms of vertical excursions of density, or whether more subtle changes in circulation are involved.

4.4.3 *Mechanisms Driving Age and Oxygen Variability*

In this section, we will use the model simulation to assess the spatial extent of the anomalous correlation outside of Line W and diagnose the most likely mechanisms responsible for the break-down in the anticipated age-AOU relationship.

4.4.3.1 *Horizontal Extent of Anomalous Correlation*

To determine the horizontal extent of the anomalous correlation between age and AOU, we show the age-AOU temporal correlation from the model on various neutral density surfaces over the entire North Atlantic basin (see left-hand side of Figure 6). These correlations show that the temporal relationship between age and AOU is largely positive throughout the entire domain with Pearson correlation coefficients exceeding XXX in most of the basin. There is a region at the end of Line W where the age-AOU correlation is reduced. This is most prominently seen on the lower neutral density surfaces (Figures 6 (e) and (g))). The subplots on the right-hand side show the correlation on each designated density surface ignoring the impacts of vertical heave in the isopycnals, while the subplots on the left side do include vertical isopycnal heave as described by the following equations:

$$r_{\text{with heave}} = \text{corr}(\Gamma, O_2)|_{\gamma_n=27.0} \quad (4.4)$$

4.4. RESULTS

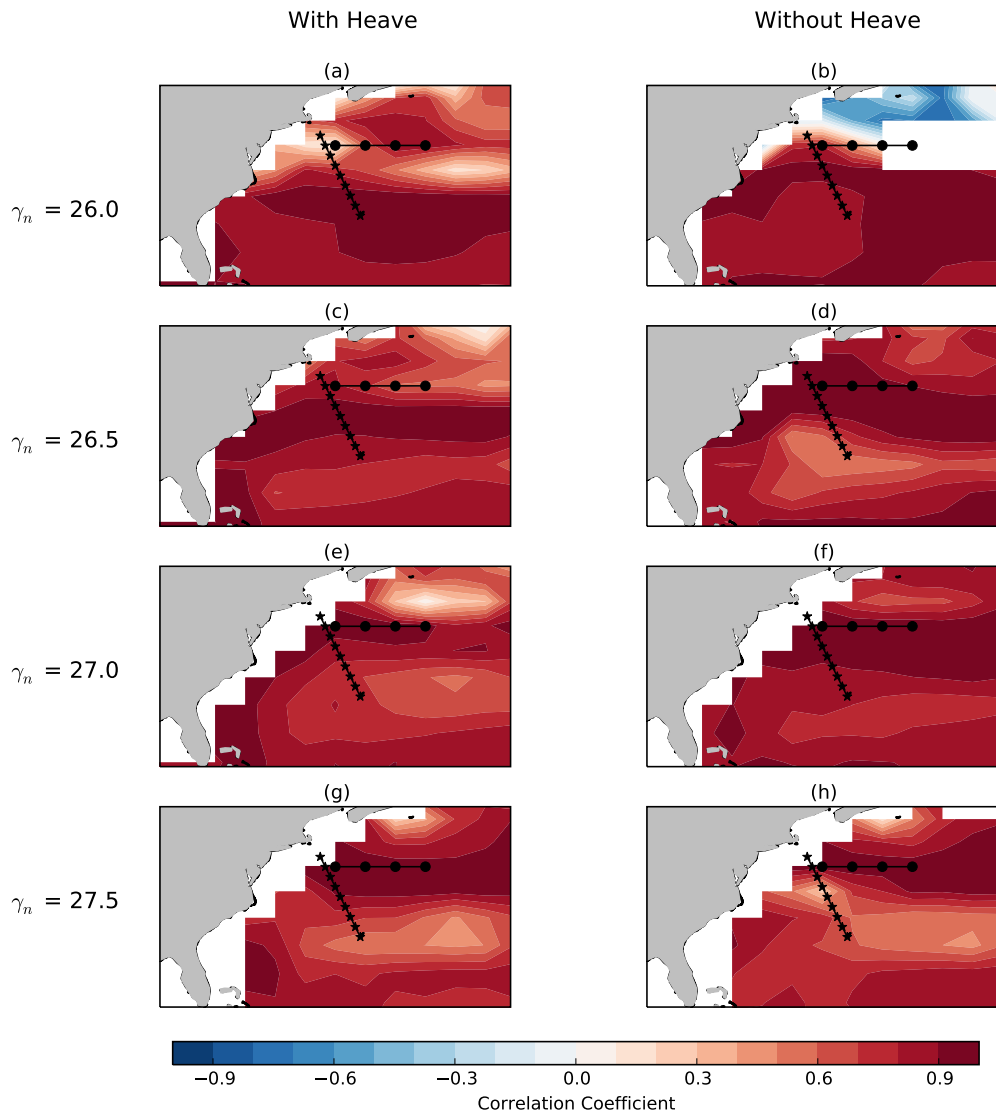


FIGURE 4.5: Correlation between age and AOU on various isopycnal surfaces. Left column indicate correlation calculated on average depth of the isopycnal surface, and therefore including contributions from isopycnal heave. Right column shows correlation calculated on the isopycnal surface and does not include contributions from heave.

$$r_{\text{without heave}} = \text{corr}(\bar{\Gamma}|_{\gamma_n=27.0}, \bar{O}_2|_{\gamma_n=27.0}) \quad (4.5)$$

In both equations (2) and (3) above, γ_n designates the depth of a neutral density surface and the overbar designates the time average. It is important to distinguish between these two methods of neutral density interpolation because the ‘with heave’ method includes the impact of vertical motion and allows us to determine the extent that vertical motion impacts the correlation. The positive correlation appears to be more significantly reduced on the neutral density surfaces including vertical heave (left-hand side subplots). These results suggest that the mechanism decoupling age and AOU is spatially limited to the region at the end of Line W and includes some component of vertical mixing.

4.4.3.2 *Line W versus Line 40N*

In order to diagnose what is causing this reduction in the negative age-oxygen correlation and positive age-AOU correlation, we examine a region of the North Atlantic where this breakdown of the age-AOU relationship does not occur and compare it with Line W. We refer to this region as Line 40N, a hypothetical transect that extends from Cape Cod eastward along latitude line 40 N. This hypothetical transect follows along a region of the North Atlantic basin where the age-oxygen correlation is strongly negative (not shown) and the age-AOU correlation is strongly positive for all neutral density surfaces (Figure 6). Comparing Line 40N and Line W allows us to evaluate the differences between the two and understand why Line W achieves these zero correlations in the age-AOU relationship. One possible reason Line 40N maintains a strong positive correlation is due to strong horizontal (primarily along-isopycnal) variability relative to Line W. In order to diagnose the relative contributions of this along-isopycnal variability and the isopycnal heave variability, we break the time rate of change of age and AOU as follows:

4.4. RESULTS

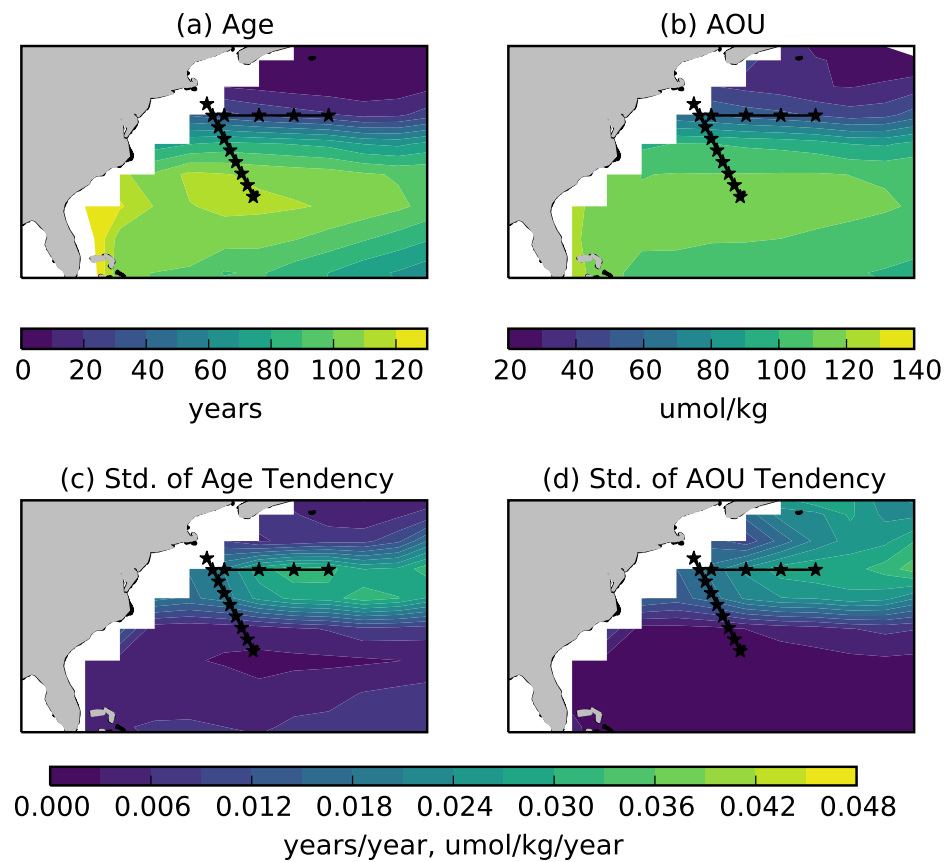


FIGURE 4.6: Climatologies of (a) age and (b) AOU interpolated on neutral density surface 27.0. Bottom: Standard deviation of (c) age tendency and (d) AOU tendency interpolated on neutral density surface 27.0. Bottom plots are calculated as the standard deviation of the first term on right-hand side of equation (4).

4.4. RESULTS

$$\frac{d\Gamma}{dt}\Big|_z = \frac{d\Gamma}{dt}\Big|_{\gamma_n=27.0} + \frac{dz}{dt}\Big|_{\gamma_n=27.0} \frac{d\Gamma}{dz} \quad (4.6)$$

$$\frac{dAOU}{dt}\Big|_z = \frac{dAOU}{dt}\Big|_{\gamma_n=27.0} + \frac{dz}{dt}\Big|_{\gamma_n=27.0} \frac{dAOU}{dz} \quad (4.7)$$

where the first term on the right-hand side refers to the age tendency on the neutral density surface and the second term on the right-hand refers to the contribution of vertical heave to the age variability. The climatologies of age and oxygen on the $n=27.0$ surface along with the standard deviation of the age and oxygen tendencies along this surface are shown in Figure 7. The end of Line W, where the age-oxygen relationship becomes positive, lies in a region where there is reduced horizontal gradient in age and oxygen. This is significantly different to Line 40N, which lies in a region where the horizontal gradients in age and oxygen (primarily in the meridional direction) are particularly strong. This results in significantly more along-isopycnal variability along Line 40N than Line W, as shown in figure 7 (c) and (d). Because of the reduced along-isopycnal variability on Line W, the vertical heave component (second term on right hand side of equations 4 and 5) may be important in setting up the reduced positive correlation between age and AOU.

To investigate the vertical heave contribution to the age-AOU correlation, we show the correlation between age and AOU for Line W and Line 40N in Figure 8. As previously discussed, Line W has an anomalous region of zero correlation. Line 40N on the other hand has a strong positive correlation between age and AOU in the upper 1500 dbars of the cross section. Figure 8 also compares the vertical profiles of age and AOU along both lines. There is a visible offset between the depths of the age and AOU maximum (as indicated by the stars) with the age maximum occurring lower in the water column (XXX depth) than the AOU maximum (XXX depth). Between the age and AOU maximums, age increases with depth and AOU decreases with depth. It is between these depths that the reduced positive correlation occurs between age and AOU (as indicated by grey shading

4.4. RESULTS

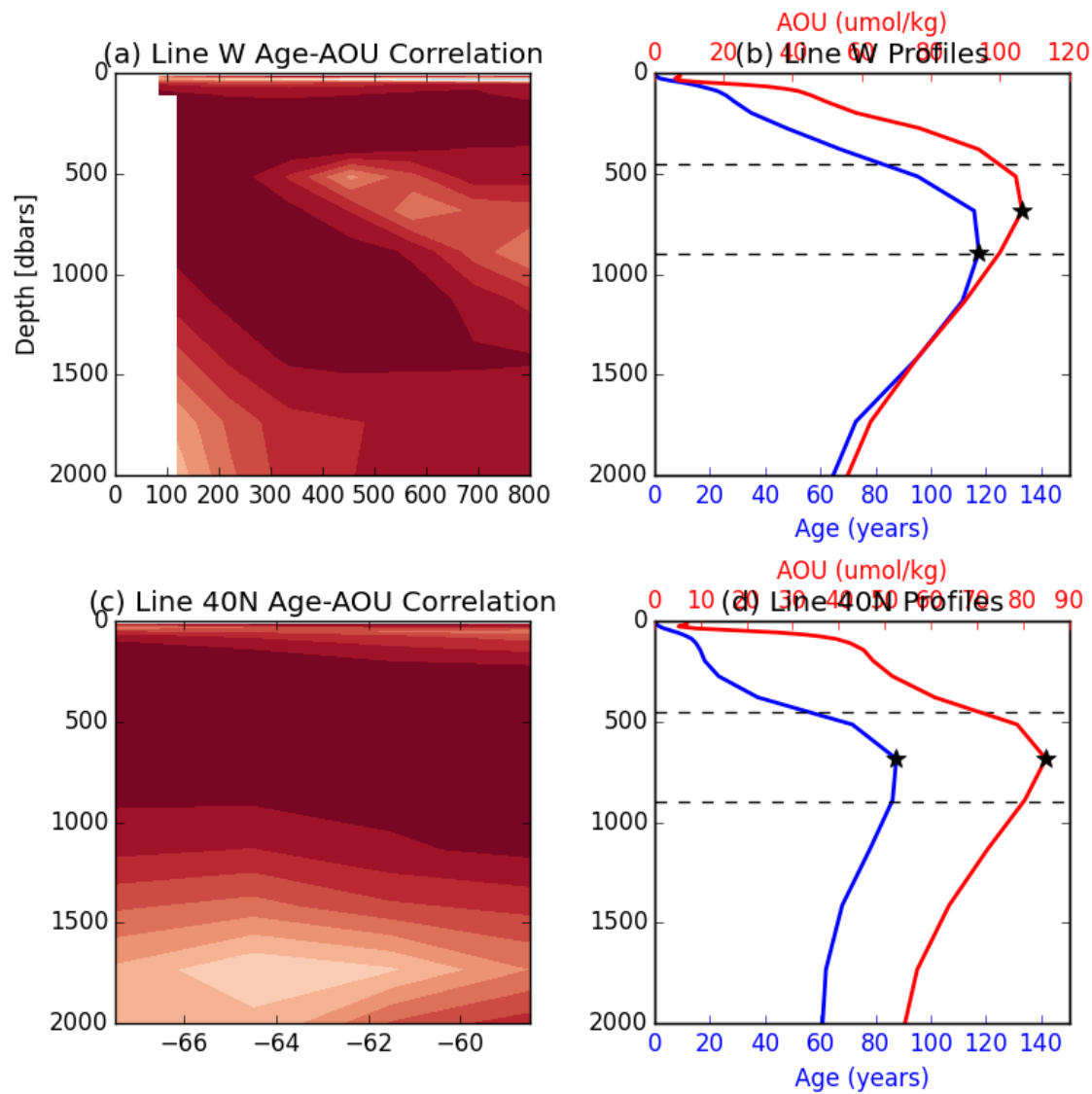


FIGURE 4.7: Age-AOU correlation and vertical profiles for (top) Line W and (bottom) Line 40N.

4.5. CONCLUSIONS

in Figure 8). We propose that the reduced correlation occurs because of vertical motion acting on this particular vertical gradient in age and AOU. When comparing the vertical profiles on Line W with Line 40N, we see that there is no offset between the age and AOU maximums on Line 40N. We also examined the magnitude of the vertical motion of the isopycnal surfaces (not shown) and found no significant difference between Line W and Line 40N. While both transects have similar levels vertical motion, the presence of a depth offset between the age and AOU maximum in addition to decreased along-isopycnal variability result in Line W having a reduced correlation between age and AOU.

Line W is unusual because the along-isopycnal (horizontal) gradients are small so that variations in mixing or along-isopycnal velocity will have relatively small impacts. This allows the vertical isopycnals heave to dominate the local variability in age and oxygen. Between depths 500 dbars - 750 dbars, this vertical heave acts on an offset in the depths of the age maximum and oxygen minimum, resulting in the observed positive correlation. In other regions of the basin (Line 40N), the horizontal mixing is large enough to dominate the local variability. Even though the same vertical heave and age maximum and oxygen minimum depth offset is seen in this region, the large magnitude of horizontal mixing maintains the expected age-oxygen relationship.

4.5 Conclusions

Our analysis of the Line W observations of age and oxygen show that there is a much more complicated relationship between the two quantities than one would naively expect. The commonly held expectation of a negative relationship between age and oxygen breaks down along observational Line W due to two regions of positive correlation. One region of positive correlation is seen within the ventilated thermocline and the other is lower in the water column. The same upper region of positive correlation is seen in an Earth System Model (GFDL ESM2Mc) representation of Line W. We additionally remove the impacts of

$$1\frac{m}{s}$$

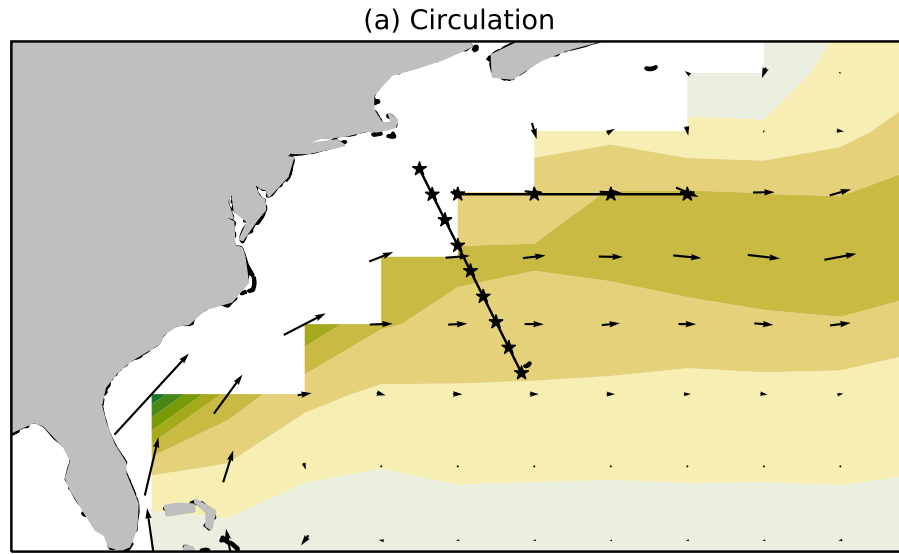


FIGURE 4.8: Circulation on neutral density surface 27.0

temperature on oxygen saturation, by looking at the age correlation with AOU. The age-AOU correlation also shows anomalous (zero to negative) correlation in the observational data set and model simulation.

Because of the limited temporal and spatial resolution of the observational data, we use the GFDL ESM2Mc to investigate the potential mechanisms causing the anomalous correlation between age and oxygen/AOU. We show that the region of anomalous correlation is limited to a region at the end of Line W, and to a few isopycnal surfaces (surfaces 27.0–27.5). The end of Line W lies in a unique region in the North Atlantic basin where the horizontal gradients in age and oxygen are relatively weak and thus the along-isopycnal variability is very small. Additionally, at the bottom of the ventilated thermocline, there is a depth offset between the age maximum and oxygen minimum resulting in a range

4.5. CONCLUSIONS

of depths where the vertical gradient in age and oxygen are the same sign. Any vertical motion within this region, coupled with the limited horizontal variability, would cause a positive correlation between the age and oxygen.

The end of Line W is unique because it lies in the approximate center of the North Atlantic gyre circulation (Figure 10). Because the horizontal circulation in the middle of the gyre is very small, there is little horizontal gradients in ocean tracers. In such regions, the balance between vertical heaving of isopycnals (which acts to decouple age-oxygen) and horizontal mixing (which mostly strengthens age-oxygen relationship) determines whether or not the expected age-oxygen relationship holds. Because of this delicate balance, one needs to consider the local dynamics before assuming that oxygen and age follow a strong negative relationship.

Bibliography

- Banks, H. T., and J. M. Gregory (2006), Mechanisms of ocean heat uptake in a coupled climate model and the implications for tracer based predictions of ocean heat uptake, *Geophysical Research Letters*, 33(7), 3–6, doi:10.1029/2005GL025352.
- Bernardello, R., I. Marinov, J. B. Palter, E. D. Galbraith, and J. L. Sarmiento (2014), Impact of Weddell Sea deep convection on natural and anthropogenic carbon in a climate model, *Geophysical Research Letters*, 41(20), 7262–7269, doi:10.1002/2014GL061313.
- Boyer, T. P., C. Stephens, J. I. Antonov, M. E. Conkright, L. A. Locarnini, T. D. O'Brien, and H. E. Garcia (2002), World Ocean Atlas 2001, *Temperature, Salinity*, 2, NOAA Atlas NESDIS 49, 165 pp, doi:<http://doi.org/10.7289/V5NZ85MT>.
- Cabré, A., I. Marinov, and A. Gnanadesikan (2017), Global atmospheric teleconnections and multi-decadal climate oscillations driven by Southern Ocean convection, *Journal of Climate*, 30, 8107–8126, doi:10.1175/JCLI-D-16-0741.1.
- Carsey, F. D. (1980), Microwave Observation of the Weddell Polynya, *Monthly Weather Review*, 108, 2031–2044.
- de Lavergne, C., J. B. Palter, E. D. Galbraith, R. Bernardello, and I. Marinov (2014), Cessation of deep convection in the open Southern Ocean under anthropogenic climate change, *Nature Climate Change*, 4(4), 278–282.
- Devries, T., M. Holzer, and F. Primeau (2017), Recent increase in oceanic carbon uptake driven by weaker upper-ocean overturning, *Nature Publishing Group*, 542(7640), 215–218, doi:10.1038/nature21068.
- Dufour, C. O., A. K. Morrison, S. M. Griffies, I. Frenger, H. Zanowski, and M. Winton (2017), Preconditioning of the Weddell Sea polynya by the ocean mesoscale and dense water overflows, *Journal of Climate*, pp. JCLI-D-16-0586.1, doi:10.1175/JCLI-D-16-0586.1.

BIBLIOGRAPHY

- Dunne, J. P., J. G. John, A. J. Adcroft, S. M. Griffies, R. W. Hallberg, E. Shevliakova, R. J. Stouffer, W. Cooke, K. A. Dunne, M. J. Harrison, J. P. Krasting, S. L. Malyshov, P. C. D. Milly, P. J. Phillipps, L. T. Sentman, B. L. Samuels, M. J. Spelman, M. Winton, A. T. Wittenberg, and N. Zadeh (2012), GFDL's ESM2 Global Coupled Climate–Carbon Earth System Models. Part I: Physical Formulation and Baseline Simulation Characteristics, *Journal of Climate*, 25(19), 2247–2267.
- Fetterer, F., K. Knowles, W. Meier, M. Savoie, and A. K. Windnagel. (2016), updated daily, *Sea Ice Index, Version 2*, pp. Boulder, Colorado USA. NSIDC: National Snow and Ice Data Center, doi: <http://dx.doi.org/10.7265/N5736NV7>.
- Frölicher, T. L., F. Joos, G. K. Plattner, M. Steinacher, and S. C. Doney (2009), Natural variability and anthropogenic trends in oceanic oxygen in a coupled carbon cycle-climate model ensemble, *Global Biogeochemical Cycles*, 23(1), doi:10.1029/2008GB003316.
- Frölicher, T. L., J. L. Sarmiento, D. J. Paynter, J. P. Dunne, J. P. Krasting, and M. Winton (2014a), Dominance of the Southern Ocean in Anthropogenic Carbon and Heat Uptake in CMIP5 Models, *Journal of Climate*, 28(2), 862–886.
- Frölicher, T. L., M. Winton, and J. L. Sarmiento (2014b), Continued global warming after CO₂ emissions stoppage, *Nature Climate Change*, 4(1), 40–44.
- Galbraith, E. D., A. Gnanadesikan, J. P. Dunne, and M. R. Hiscock (2010), Regional impacts of iron-light colimitation in a global biogeochemical model, *Biogeosciences*, 7, 1043–1064, doi:10.5194/bgd-6-7517-2009.
- Galbraith, E. D., E. Y. Kwon, A. Gnanadesikan, K. B. Rodgers, S. M. Griffies, D. Bianchi, J. L. Sarmiento, J. P. Dunne, J. Simeon, R. D. Slater, A. T. Wittenberg, and I. M. Held (2011), Climate Variability and Radiocarbon in the CM2Mc Earth System Model, *Journal of Climate*, 24(16), 4230–4254.
- Galbraith, E. D., J. P. Dunne, A. Gnanadesikan, R. D. Slater, J. L. Sarmiento, C. O. Dufour, G. F. de Souza, D. Bianchi, M. Claret, K. B. Rodgers, and S. S. Marvasti (2015), Coupled functionality with minimal computation: Promise and pitfalls of reduced-tracer ocean biogeochemistry models, *Journal of Advances in Modeling Earth Systems*, 7, 2012–2028, doi:10.1002/2015MS000463.
- Gent, P. R., and J. C. McWilliams (2010), Isopycnal Mixing in Ocean Circulation Models, *Journal of Physical Oceanography*, 20(1), 150–155.
- Gent, P. R., J. Willebrand, T. J. McDougall, and J. C. McWilliams (1995), Parameterizing Eddy-Induced Tracer Transports in Ocean Circulation Models, dx.doi.org/10.1029/94JC02504, 25(4), 463–474.
- Gnanadesikan, A., M.-A. Pradal, and R. P. Abernathey (2015), Isopycnal mixing by mesoscale eddies significantly impacts oceanic anthropogenic carbon uptake, *Geophysical Research Letters*, 42(11), 4249–4255, doi:10.1002/2015GL064100.
- Gordon, A. L. (1982), Weddell Deep Water variability, *Journal of Marine Research*, 40, 199–217.

BIBLIOGRAPHY

- Griffies, S. M., M. Winton, W. G. Anderson, R. Benson, T. L. Delworth, C. O. Dufour, J. P. Dunne, P. Goddard, A. K. Morrison, A. Rosati, A. T. Wittenberg, J. Yin, and R. Zhang (2015), Impacts on Ocean Heat from Transient Mesoscale Eddies in a Hierarchy of Climate Models, *Journal of Climate*, 28, 952–977, doi:10.1175/JCLI-D-14-00353.1.
- Gruber, N., J. Sarmiento, and T. Stocker (1996), An improved method for detecting anthropogenic CO₂ in the oceans, *Global Biogeochemical Cycles*, 10(4), 809–837, doi:doi:10.1029/96GB01608.
- Khatiwala, S., F. Primeau, and M. Holzer (2012), Ventilation of the deep ocean constrained with tracer observations and implications for radiocarbon estimates of ideal mean age, *Earth and Planetary Science Letters*, 325–326, 116–125.
- Landschutze, P., N. Gruber, F. A. Haumann, R. Christian, D. C. E. Bakker, S. V. Heuven, M. Hoppema, N. Metzl, C. Sweeney, and T. Takahashi (2015), The Reinvigoration of the Southern Ocean Carbon Sink, *Science*, 349(6253), 1221–1224, doi:10.1126/science.aaa2620.
- Latif, M., T. Martin, and W. Park (2013), Southern Ocean Sector Centennial Climate Variability and Recent Decadal Trends, *Journal of Climate*, 26(19), 7767–7782.
- Le Quere, C., J. C. Orr, P. Monfray, and O. Aumont (2000), Interannual variability of the oceanic sink of CO₂ from 1979 through 1997, *Global Biogeochemical Cycles*, 14(4), 1247–1265.
- Lenton, A., F. Codron, L. Bopp, N. Metzl, P. Cadule, A. Tagliabue, and J. L. Sommer (2009), Stratospheric ozone depletion reduces ocean carbon uptake and enhances ocean acidification, *Geophysical Research Letters*, 36, 1–5, doi:10.1029/2009GL038227.
- Levitus, S., J. I. Antonov, T. P. Boyer, R. A. Locarnini, H. E. Garcia, and A. V. Mishonov (2009), Global ocean heat content 1955–2008 in light of recently revealed instrumentation problems, *Geophysical Research Letters*, 36(7), 1–5, doi:10.1029/2008GL037155.
- Lovenduski, N. S., N. Gruber, S. C. Doney, and I. D. Lima (2007), Enhanced CO₂ outgassing in the Southern Ocean from a positive phase of the Southern Annular Mode, *Global Biogeochemical Cycles*, 21(2), doi:10.1029/2006GB002900.
- Marinov, I., A. Gnanadesikan, J. L. Sarmiento, J. R. Toggweiler, M. Follows, and B. K. Mignone (2008), Impact of oceanic circulation on biological carbon storage in the ocean and atmospheric pCO₂, *Global Biogeochemical Cycles*, 22(3), n/a–n/a.
- Martinson, D. G., P. D. Killworth, and A. L. Gordon (1981), A Convective Model for the Weddell Polynya, *Journal of Physical Oceanography*, 11, 466–488.
- Ollitrault, M., and A. Colin de Verdière (2002), SOFAR Floats Reveal Midlatitude Intermediate North Atlantic General Circulation. Part I: A Lagrangian Descriptive View, *Journal of Physical Oceanography*, 32(7), 2020–2033.

BIBLIOGRAPHY

- Pradal, M.-A., and A. Gnanadesikan (2014), How does the Redi parameter for mesoscale mixing impact global climate in an Earth System Model?, *Journal of Advances in Modeling Earth Systems*, 6(3), 586–601, doi:10.1002/2013MS000273.
- Purkey, S. G., and G. C. Johnson (2012), Global contraction of Antarctic Bottom Water between the 1980s and 2000s, *Journal of Climate*, 25(17), 5830–5844, doi:10.1175/JCLI-D-11-00612.1.
- Redi, M. H. (1982), Oceanic Isopycnal Mixing by Coordinate Rotation, *Journal of Physical Oceanography*, 12, 1154–1158.
- Russell, A. M., and A. Gnanadesikan (2014), Understanding multidecadal variability in ENSO amplitude, *Journal of Climate*, 27(11), 4037–4051, doi:10.1175/JCLI-D-13-00147.1.
- Sabine, C. L., R. A. Feely, N. Gruber, R. M. Key, L. Kitack, J. L. Bullister, R. Wanninkhof, C. S. Wong, D. W. R. Wallace, B. Tilbrook, F. J. Millero, T.-H. Peng, A. Kozyr, T. Ono, and A. F. Rios (2004), The Oceanic Sink for Anthropogenic CO₂, *Science*, 305, 367–371.
- Sarmiento, J. L., and C. Le Quere (1996), Oceanic Carbon Dioxide Uptake in a Model, *Science*, 274, 1346–1350.
- Sarmiento, J. L., and J. R. Toggweiler (1984), A new model for the role of the oceans in determining atmospheric pCO₂, *Nature*.
- Seviour, W. J. M., A. Gnanadesikan, D. W. Waugh, and M.-A. Pradal (2017), Transient response of the Southern Ocean to changing ozone: Regional responses and physical mechanisms, *Journal of Climate*, pp. JCLI-D-16-0474.1, doi:10.1175/JCLI-D-16-0474.1.
- Thomas, J. L., D. W. Waugh, and A. Gnanadesikan (2015), Southern Hemisphere extratropical circulation: Recent trends and natural variability, *Geophysical Research Letters*, 42(13), 5508–5515.
- Waugh, D. W., T. M. Hall, B. I. McNeil, R. Key, and R. J. Matear (2006), Anthropogenic CO₂ in the oceans estimated using transit time distributions, *Tellus B*, 58(5), 376–389.
- Waugh, D. W., F. Primeau, T. DeVries, and M. Holzer (2013), Recent Changes in the Ventilation of the Southern Oceans, *Science*, 339(6119), 568–570.
- Winton, M., S. M. Griffies, B. L. Samuels, J. L. Sarmiento, and T. L. Frölicher (2013), Connecting Changing Ocean Circulation with Changing Climate, *Journal of Climate*, 26(7), 2268–2278.
- Xie, P., and G. K. Vallis (2012), The passive and active nature of ocean heat uptake in idealized climate change experiments, *Climate Dynamics*, 38(3-4), 667–684, doi:10.1007/s00382-011-1063-8.

Jordan Thomas

Born: May 4, 1990

Wichita, KS

Education

Johns Hopkins University (August 2012 – Present)	Baltimore, MD
PhD in Earth and Planetary Science	
Masters in Earth and Planetary Science	
Dissertation: Investigating Natural Variability in the Climate System	
Pennsylvania State University (August 2008– May 2012)	University Park, PA
Bachelors of Science in Meteorology	
Concentration in Atmospheric Sciences	
University of Southampton (January 2011 – July 2011)	Southampton, UK
Minor in Oceanography	

Publications

- Thomas J. L., Waugh D. W., and Gnanadesikan A. (2018) “Relationship between ocean heat and carbon variability”. *Journal of Climate*. 31. 1467–1482.
- Brune W. H., Baier B. C., Thomas J.L., Ren X., Cohen R. C., Pusede S. E., Browne E. C., Goldstein A. H., Gentner D. R., Keutsch F. N., Thornton J.A., Harrold S., Lopez-Hilfiker F. D. and Wennberg P. O. (2016) “Ozone production chemistry in the presence of urban plumes”. *Faraday Discussions*. 189. 169–189.
- Thomas J. L., Waugh D. W., and Gnanadesikan A. (2015) “Southern Hemisphere extra-tropical circulation: Recent trends and natural variability”. *Geophysical Research Letters*. 42. 5508–5515.
- Pusede S. E., Gentner D. R., Wooldridge P. J., Browne E. C., Rollins A. W., Min K.-E., Russell A. R., Thomas J. L., Zhang L., Brune W. H., Henry S. B., DiGangi J. P., Keutsch F. N., Harrold S. A., Thornton J. A., Beaver M. R., St. Clair J. M., Wennberg P. O., Sanders J., Ren X., VandenBoer T. C., Markovic M. Z., Guha A., Weber R., Goldstein A. H., and Cohen R. C. (2014) “On the temperature dependence of organic reactivity, nitrogen oxides, ozone production, and the impact of emission controls in San Joaquin Valley, California”. *Atmospheric Chemistry and Physics*. 14. 3373–3395.

Experience

Johns Hopkins University | RESEARCH ASSISTANT

September 2012 – Present

- Researched the impact of ozone depletion on atmospheric and oceanic circulation biogeochemistry.
- Performed statistical analysis on output from 27 coupled climate model simulations (CMIP5) using Python to determine that recent trends in atmospheric quantities are likely caused by anthropogenic activities.
- Designed and executed model simulations using a fully coupled General Circulation Model to investigate relationship between ocean heat and carbon content.
- Analyzed model output using post-processing techniques in Python and MATLAB, focusing on atmosphere-ocean interactions, ocean dynamics, ocean biogeochemistry and ocean acidification.
- Presented dissertation research at multiple scientific conferences and invited talks including at University of Pennsylvania and MIT.

Johns Hopkins University | TEACHING ASSISTANT

September 2015 – December 2015

- Developed and taught interactive lessons focused on global and environmental change.
- Facilitated bi-weekly review sessions and held weekly office hours to assist with questions and homework.

Pennsylvania State University | UNDERGRADUATE RESEARCH ASSISTANT

August 2009 – May 2012

- One of two students selected from Penn State to participate in CalNEX 2010, an air quality research campaign in Bakersfield, CA.
- Studied oxidation photochemistry and preformed analysis and model comparison with collected data.
- Developed an instrument to measure in-situ tropospheric ozone production.
- Analyzed air-quality data to diagnose large scale meteorological patters.